

Controlled Evaluation of Metal-Based Nanomaterial Transformations

Ronald D. Kent

Dissertation submitted to the faculty of the Virginia Polytechnic Institute and State University in
partial fulfillment of the requirements for the degree of

Doctor of Philosophy
In
Civil Engineering

Peter J. Vikesland, Chair
Andrea M. Dietrich
Patricia M. Dove
Linsey C. Marr

June 3, 2015
Blacksburg, VA

Keywords: Nanomaterials, silver, copper, oxidation, dissolution, sulfidation, nanosphere
lithography, fate, transformations, convective self-assembly, atomic force microscopy

Controlled Evaluation of Metal-Based Nanomaterial Transformations

Ronald D. Kent

ABSTRACT

Metal-based nanoparticles (MNPs) are becoming increasingly common in commercial products. Release of these materials into the environment raises concerns about the potential risks they pose to aquatic life. Predicting these risks requires an understanding of MNPs' chemical transformations. In this study, arrays of immobilized MNPs fabricated by nanosphere lithography (NSL) were used to investigate environmental transformations of MNPs. Specifically, sulfidation of silver nanoparticles (Ag NPs) and dissolution of copper-based nanoparticles (Cu NPs) were investigated. Atomic force microscopy (AFM) and transmission electron microscopy were the primary analytical techniques for these investigations. Because the MNPs were immobilized on a solid surface, the samples were field deployable, environmentally relevant metal concentrations were maintained, and the confounding influence of MNP aggregation was eliminated. Ag NP samples were deployed in a full-scale wastewater treatment plant. Sulfidation occurred almost exclusively in anaerobic zones of the WWTP, where the initial sulfidation rate was 11-14 nm of Ag converted to Ag₂S per day. Conversion to Ag₂S was complete within 7-10 d. Dissolution rates of Cu-based NPs were measured *in situ* over a range of pH by flow-cell AFM. Based on the measured rates, CuO/Cu(OH)₂ NPs dissolve completely within a matter of hours at any pH, metallic Cu NPs persist for a few hours to days, and Cu_xS NPs do not dissolve significantly over the time scales studied. Field deployment of samples in a freshwater stream confirmed these conclusions for a natural aquatic system. This research demonstrates that environmental transformations of MNPs will be a key factor in determining the ultimate form and concentration of NPs that aquatic organisms will be exposed to.

Acknowledgements

I thank my advisor, Dr. Peter Vikesland, for his insight, guidance, and innovative ideas throughout my time at Virginia Tech, and for giving me the opportunity to work on this research project. He was ready and available to help whenever I needed his input. I also thank the other members of my committee, Dr. Andrea Dietrich, Dr. Patricia Dove, and Dr. Linsey Marr, for their support of my dissertation work. I thank the staff at the Nanoscale Characterization and Fabrication Laboratory, especially Stephen McCartney, Chris Winkler, Andrew Giordani, and Mitsu Murayama, for their assistance with SEM, TEM, and XPS. I am grateful to Stefan Stoianov, Erich See, and Hans Robinson for their assistance with producing NSL arrays. Jeff Parks and Jody Smiley provided lab support for ICP-MS and TOC analysis for which I am grateful. I am deeply grateful to my family. I could never have received an advanced education without the assistance that my parents, Robert and Linda Kent, have provided to me throughout my life. My wife, Katie Kent, has been a continual source of strength to me. Her patience and loving support has carried me through the challenges of graduate school. I gratefully acknowledge the financial support of a Ph.D. Via Fellowship from the Charles Edward Via, Jr. Department of Civil and Environmental Engineering at Virginia Tech and a Science to Achieve Results (STAR) fellowship from the United States Environmental Protection Agency (EPA). Funding for this project was provided by National Science Foundation (NSF) Grant 1411385 and the Center for the Environmental Implications of NanoTechnology (CEINT), which is supported by NSF and the EPA.

Table of Contents

List of Figures.....	vi
List of Tables.....	viii
1 Introduction.....	1
1.1 Overview.....	1
1.2 Attribution.....	2
References.....	3
2 Controlled Evaluation of Silver Nanoparticle Sulfidation in a Full-Scale Wastewater Treatment Plant.....	4
2.1 Abstract.....	4
2.2 Introduction.....	5
2.3 Materials and Methods.....	7
2.3.1 Substrate Production.....	7
2.3.2 Analytical Techniques.....	8
2.3.3 Sulfidation and Dissolution Laboratory Experiments.....	9
2.3.4 Field Deployment in a Wastewater Treatment Plant.....	10
2.4 Results and Discussion.....	11
2.4.1 Laboratory Study of Sulfidation.....	11
2.4.2 Field Deployment in a Wastewater Treatment Plant.....	17
2.4.3 Environmental Implications.....	20
References.....	22
Figures.....	25
3 Dissolution and Persistence of Copper-Based Nanomaterials in Unsaturated Solutions.....	31
3.1 Abstract.....	31
3.2 Introduction.....	31
3.3 Materials and Methods.....	34
3.3.1 Sample Preparation.....	34
3.3.2 Ozone and Sulfide Treatments.....	35
3.3.3 Sample Characterization.....	35
3.3.4 Dissolution Experiments.....	36
3.3.5 Field Deployment.....	37
3.4 Results and Discussion.....	38
3.4.1 Dissolution Kinetics Model.....	39
3.4.2 Nanomaterial Characterization.....	43

3.4.3	Nanomaterial Dissolution	47
3.4.4	Estimated Concentrations	49
3.4.5	Field Deployment in a Freshwater Creek	51
3.5	Conclusions	53
	References	55
	Figures	59
4	Conclusions	66
	Appendix A: Supplemental Information for Chapter 2	68
	Appendix B: Supplemental Information for Chapter 3	81
	Appendix C: Ion Diffusion in Batch Dissolution Experiments	91

List of Figures

Figure 2-1. A) SEM and B) AFM images of unsulfidized Ag NP arrays produced by NSL. C) AFM image of an Ag NP array after a 2-d exposure to 10 μM Na_2S . D) Ag NP height distributions before (black) and after (red) the exposure.	25
Figure 2-2. A) Bright field TEM image of NSL-produced Ag NPs after a 2-d exposure to 10 μM sodium sulfide. Particles I and II are indicated in the circles. B) EDS spectrum from Particle I.	26
Figure 2-3. A) Dark field TEM image of Particle II (see Figure 2-2A). B) High resolution TEM image of the area marked in A. FFTs from C) Crystal I and D) Crystal II.	27
Figure 2-4. Mean height measured by AFM over time for Ag NPs exposed to 550 mM NaCl (pH 6.0). Prior to exposure to the NaCl solution, particles were exposed to 1 mM Na_2S for 0, 5, 15, or 30 min. Error bars represent standard deviations of triplicate measurements. Inset: Dissolution rates calculated by linear regression for the different sulfidation times. Error bars indicate 95% confidence intervals.	28
Figure 2-5. Ratio of mean height (h) to initial mean height (h_0) measured over time by AFM for Ag NP arrays deployed in A) anoxic and aerobic zones of an activated sludge basin on March 24-30, 2014 and B) primary and secondary clarifiers on April 21-30, 2014. Error bars represent standard deviations of triplicate samples.	29
Figure 2-6. A) Bright field TEM image of NSL-produced Ag NPs after a 10-d exposure in the primary influent of the Christiansburg WWTP. B) High resolution TEM image of the region marked by the larger square in A. C) High resolution TEM image of the region marked by the smaller square in A. D) FFT of the image in C.	30
Figure 3-1. SEM micrographs of A) Cu, B) $\text{CuO}/\text{Cu}(\text{OH})_2$, and C) Cu_xS NPs. D) Height distributions of Cu (blue), $\text{CuO}/\text{Cu}(\text{OH})_2$ (red), and Cu_xS (green) NPs measured by AFM.	59
Figure 3-2. Bright field STEM images of A) Cu NPs, D) $\text{CuO}/\text{Cu}(\text{OH})_2$ NPs, and G) Cu_xS NPs. Inset: SAED pattern from the respective sample. EDS maps of B) Cu and C) O for Cu NPs, E) Cu and F) O for $\text{CuO}/\text{Cu}(\text{OH})_2$ NPs, and H) Cu and I) S for Cu_xS NPs.	60
Figure 3-3. XPS spectra of A) Cu, B) $\text{CuO}/\text{Cu}(\text{OH})_2$, and C) Cu_xS NPs in the Cu 2p region. D) XPS spectra of Cu_xS NPs in the S 2p region.	61
Figure 3-4. Representative AFM height images and cross-sections of Cu NPs A) before and B) after 6 h, $\text{CuO}/\text{Cu}(\text{OH})_2$ NPs C) before and D) after 1 h, and Cu_xS NPs E) before and F) after 6 h in DI water (pH 5.6) with a 2 mL/min flow rate. Heights in cross sections are all in units of nm.	62
Figure 3-5. Representative time series of Cu-based NP mean heights measured by AFM under a 2 mL/min flow rate at pH A) 5.6, B) 6.6, C) 8.4, and D) 11.3.	63
Figure 3-6. A) Dissolution rate constants and B) surface area normalized dissolution rates for Cu and $\text{CuO}/\text{Cu}(\text{OH})_2$ NPs at various pH. Error bars represent standard errors from at least triplicate experimental runs. Particle lifetime as a function of initial diameter for C) Cu and D) $\text{CuO}/\text{Cu}(\text{OH})_2$ NPs (note the different vertical scales).	64
Figure 3-7. Change in mean height of Cu, $\text{CuO}/\text{Cu}(\text{OH})_2$, and Cu_xS NPs over time in Stroubles Creek. Error bars represent standard deviations of triplicate specimens.	65
Figure A-1. A) High resolution TEM image of an unsulfidized Ag NP produced by NSL. B) FFT of A.	73

Figure A-2. A) Bright field TEM image of an unsulfidized Ag NP produced by NSL. B-D) Dark field TEM images of the particle shown in A.	74
Figure A-3. A) Bright field TEM image of an unsulfidized Ag NP array produced by NSL. B) High resolution TEM image of one of the small (2-10 nm) Ag NPs produced by NSL. C) FFT of the particle shown in B.	75
Figure A-4. A and C) High resolution TEM images of Particle I (Figure 2-2A). B and D) FFTs of the regions marked in A and C, respectively.	76
Figure A-5. Ag NPs produced by NSL A) before and B) after a 6-d exposure to sewage sludge.	77
Figure A-6. A) Ratio of mean height (h) to initial mean height (h_0) measured over time by AFM for Ag NP arrays exposed to sludge from a municipal wastewater treatment plant. B) Mean height measured over time for Ag NPs exposed to 500 mM NaCl following a 6-d exposure to sludge. Error bars represent standard deviations of triplicate measurements.	78
Figure A-7. A) Bright field TEM image of NSL-produced Ag NPs after a 2-d exposure to sludge from a municipal wastewater treatment plant. B) EDS spectrum and C) high resolution TEM image of the particle circled in A. D) FFT of the region marked in C.	79
Figure A-8. A) SEM image of Ag NPs that had been deployed in the anoxic zone of the activated sludge basin of the WWTP for 7 d. B) Background EDS spectrum (black) and EDS spectrum of the small aggregate circled in A (red).	80
Figure B-1. Time series of mean heights measured by AFM for two CuO/Cu(OH) ₂ specimens (pH 5.6, 2 mL/min flow rate).	87
Figure B-2. XPS spectra of the C 1s binding region.	88
Figure B-3. Modeled concentrations of total dissolved Cu ²⁺ for A) Cu NPs and B) CuO/Cu(OH) ₂ NPs.	89
Figure C-1. A) Modeled dissolved Ag ⁺ concentration profiles at various times along the longitudinal axis of a sample tube during a batch dissolution experiment with $k = 2.2$ nm/d. B) Modeled dissolved Ag ⁺ concentration as a function of time at the sample surface (i.e., at $x = 0$) for various dissolution rate constants.	94

List of Tables

Table B-1. Comparison of Dissolved Concentrations and Solubility	90
--	----

1 Introduction

1.1 OVERVIEW

Metal-based nanoparticles (MNPs) are a class of emerging contaminants that are of concern because of their potential ecotoxicity.^{1,2} To mitigate the risks of MNP release, their environmental transformations must be understood.³ Sulfidation and dissolution are key processes that will impact the fate of MNPs in the environment.⁴⁻⁶ Nanosphere lithography (NSL)⁷ was chosen to fabricate regular arrays of immobilized MNPs, and atomic force microscopy (AFM) was used as the primary method to monitor MNP transformations. Several distinct advantages are realized by this methodology. First, attachment of MNPs to a macroscopic surface makes the samples field deployable. The samples can be studied by AFM, transmission electron microscopy (TEM), and other techniques before and after field deployment at varied time intervals to learn about the kinetics of transformation reactions. The regular NSL pattern also facilitates these field studies by making the primary particles clearly distinguishable from secondary particles and other debris that attaches to the deployed substrate. Second, a very low total mass of MNPs can be utilized for experiments. Studies of nanomaterial fate and toxicity in the environment often employ unrealistically high concentrations, which is a significant stumbling block to understanding the actual behavior of MNPs in real-world environments. The low total MNP mass of the NSL-produced specimens made it possible to investigate MNP transformations under environmentally relevant concentrations. Finally, attachment of MNPs to a solid support prevents aggregation. Efforts to fundamentally understand chemical transformations can be confounded by a concurrent aggregation process. The elimination of aggregation as a confounding variable provided this research with a clear

view of the transformations of interest. These advantages combined in this project to produce clear, environmentally relevant results that elucidated the fate of MNPs in natural waters.

Three chapters follow this introductory chapter. Chapter 2 reports on the field deployment of Ag NP specimens in a full-scale wastewater treatment plant and a related laboratory study of Ag NP sulfidation. Chapter 3 presents original research using flow-cell AFM to study the dissolution rates of Cu-based NPs in undersaturated solutions and a field-scale dissolution experiment in a freshwater stream. The final chapter summarizes the major conclusions of the work performed for this dissertation.

1.2 ATTRIBUTION

Ronald D. Kent is the primary author of this dissertation. He performed most of the lab work, designed experiments, performed analyses, interpreted results, and wrote the bulk of this document. Dr. Peter J. Vikesland is coauthor of Chapter 2, Chapter 3, Appendix A, and Appendix B. He made significant edits to drafts of these chapters. Dr. Vikesland also made important intellectual contributions to this work as a whole. Joel G. Oser is coauthor of Chapter 2 and Appendix A. He performed the AFM measurements for laboratory Ag NP exposures to raw sewage sludge and wrote an initial draft of the section discussing the results.

REFERENCES

1. Griffitt, R. J.; Luo, J.; Gao, J.; Bonzongo, J. C.; Barber, D. S. Effects of Particle Composition and Species on Toxicity of Metallic Nanomaterials in Aquatic Organisms. *Environ. Toxicol. Chem.* **2008**, *27*, 1972-1978.
2. Klaine, S. J.; Alvarez, P. J. J.; Batley, G. E.; Fernandes, T. F.; Handy, R. D.; Lyon, D. Y.; Mahendra, S.; McLaughlin, M. J.; Lead, J. R. Nanomaterials in the Environment: Behavior, Fate, Bioavailability, and Effects. *Environ. Toxicol. Chem.* **2008**, *27*, 1825-1851.
3. Lowry, G. V.; Gregory, K. B.; Apte, S. C.; Lead, J. R. Transformations of Nanomaterials in the Environment. *Environ. Sci. Technol.* **2012**, *46*, 6893-6899.
4. Levard, C.; Hotze, E. M.; Lowry, G. V.; Brown, G. E. Environmental Transformations of Silver Nanoparticles: Impact on Stability and Toxicity. *Environ. Sci. Technol.* **2012**, *46*, 6900-6914.
5. Liu, J. Y.; Hurt, R. H. Ion Release Kinetics and Particle Persistence in Aqueous Nano-Silver Colloids. *Environ. Sci. Technol.* **2010**, *44*, 2169-2175.
6. Wang, Z.; von dem Bussche, A.; Kabadi, P. K.; Kane, A. B.; Hurt, R. H. Biological and Environmental Transformations of Copper-Based Nanomaterials. *ACS Nano* **2013**, *7*, 8715-8727.
7. Haynes, C. L.; Van Duyne, R. P. Nanosphere Lithography: A Versatile Nanofabrication Tool for Studies of Size-Dependent Nanoparticle Optics. *J. Phys. Chem. B* **2001**, *105*, 5599-5611.

2 Controlled Evaluation of Silver Nanoparticle Sulfidation in a Full-Scale Wastewater Treatment Plant

Reprinted with permission from Kent, R. D.; Oser, J. G.; Vikesland, P. J., Controlled Evaluation of Silver Nanoparticle Sulfidation in a Full-Scale Wastewater Treatment Plant. *Environ. Sci. Technol.* **2014**, *48* (15), 8564-8572. Copyright 2014 American Chemical Society.

2.1 ABSTRACT

Sulfidation of silver nanoparticles (Ag NPs), which is known to alter Ag NP toxicity, occurs during transport through wastewater treatment plants. In this study, arrays of immobilized Ag NPs fabricated by nanosphere lithography (NSL) were used to study Ag NP sulfidation in a full-scale wastewater treatment plant (WWTP). A detailed laboratory study preceded field deployment. The characteristic NSL pattern remained discernible by atomic force microscopy and transmission electron microscopy after both lab and field exposures. Growth of Ag NPs due to a decrease in density upon sulfidation permitted the study of sulfidation kinetics in the WWTP. Sulfidation occurred almost exclusively in anaerobic zones of the WWTP, where the initial sulfidation rate was 11-14 nm of Ag converted to Ag₂S per day. Measurements of the chemical composition and crystallinity of Ag NPs exposed to primary influent for ~10 d confirmed that they had been converted almost entirely to Ag₂S. Laboratory experiments revealed that the sulfidation process is not uniform and that partially sulfidized Ag NPs retain the potential to release toxic Ag⁺ ions. The results indicate that primary Ag NPs are sulfidized directly without dissolving and forming secondary precipitates. This study demonstrates the utility of immobilized Ag NPs for detailed, *in situ* investigations of nanomaterial transformations.

2.2 INTRODUCTION

Silver nanoparticles (Ag NPs) have been incorporated into commercial products at a growing rate in recent years. Their broad application primarily stems from their potent antimicrobial properties.¹⁻³ These same properties have led many to raise concerns about the potential release of Ag NPs to the environment. Indeed, research has demonstrated likely routes of Ag NP release to aquatic environments and the potential toxic effects of Ag NPs on aquatic organisms.^{4,7} These toxic effects arise, at least in part, from oxidation and dissolution reactions that make harmful Ag^+ ions available for biouptake.⁸⁻¹⁰

Once Ag NPs are released from products, they are generally expected to travel through municipal sewer lines and wastewater treatment plants (WWTPs) prior to entering the natural environment.¹¹ Anaerobic conditions are common in wastewater, so hydrogen sulfide concentrations can be particularly high in these systems.¹² The discovery of Ag_2S nanoparticles in the final sewage sludge of a full-scale WWTP demonstrated that silver is likely to become sulfidized as it travels through wastewater infrastructure.¹³ Others showed that Ag NPs were converted to Ag_2S during transport through a pilot-scale wastewater treatment plant.¹⁴ There is also evidence that the sulfidation process begins in urban sewer systems prior to arrival at WWTPs.¹⁵

Sulfidation of Ag NPs that travel through wastewater infrastructure may alleviate their potential ecological harm. Because the solubility of Ag_2S is low ($K_{\text{sp}} = 5.92 \times 10^{-51}$), sulfidation is expected to reduce Ag NP toxicity by decreasing Ag^+ release from particle surfaces.¹¹ In one study, Ag^+ release in Ag NP suspensions was diminished upon addition of Na_2S until it was undetectable at concentrations near stoichiometric ratios of S:Ag.¹⁶ Others have shown that Ag_2S in sewage sludge resists oxidation even after six months of simulated stockpiling and

composting.¹⁷ Additionally, sulfidized Ag NPs inhibited growth of *Escherichia coli* to a lesser extent than unsulfidized Ag NPs, with intermediate growth inhibition for partially sulfidized Ag NPs.¹⁸ Inhibition of an enrichment culture of nitrifying bacteria by Ag NPs was also mitigated by the addition of sulfide.¹⁹

Ag NPs may be converted to Ag₂S either by a direct heterogeneous reaction or by a dissolution/precipitation mechanism.¹² The former mechanism implies that Ag⁺ ions will be sequestered by sulfides before they become bioavailable, but the latter mechanism allows Ag⁺ to be temporarily available for biouptake.¹² The literature has been somewhat contradictory on which mechanism is more important.^{12, 16, 18} It has been suggested that the HS⁻:Ag molar ratio affects the sulfidation process;¹⁸ however, investigations of the sulfidation mechanism have used very low HS⁻:Ag molar ratios (0.01-2.02)^{12, 16, 18} compared to what is expected in the environment (~2-16,000).^{12, 20} Because the environmental relevance of such experiments is questionable, there has been a growing interest in using field deployable samples to study the environmental transformations of Ag NPs. For example, Ag NPs have been embedded in agarose gel and immobilized on substrates to enable field studies of their environmental transformations in lakes, rivers, and a marina.^{21, 22}

Herein, we report the field deployment of immobilized Ag NPs in a full-scale WWTP. We produced uniform periodic arrays of Ag NPs on glass substrates and transmission electron microscopy (TEM) grids by nanosphere lithography (NSL).^{23, 24} NSL relies on hexagonally close packed monolayers of colloidal spheres as a lithographic mask. Metal vapor is deposited onto the mask and leaves a periodic array of metallic nanoparticles with a truncated tetrahedral shape once the mask is removed. Atomic force microscopy (AFM) and TEM were used to study changes in the morphology, chemical composition, and crystal structure of these Ag NP arrays.

Detailed laboratory studies were performed prior to field deployment. The results demonstrate the utility of this technique for studying the kinetics and mechanisms of environmental transformations of nanomaterials at complex field sites.

2.3 MATERIALS AND METHODS

2.3.1 Substrate Production

Glass substrates (60 × 24 × 0.15 mm cover glass, Fisher Scientific) were cleaned by immersion in an aqueous solution of 4% NH₄OH and 16% H₂O₂ at 75 °C for 10 min followed by immersion in 14% HCl and 14% H₂O₂ at 75 °C for 10 min. The substrates were rinsed thoroughly with DI water after each cleaning step and stored in DI water until further use. Convective self-assembly (CSA) was performed by the method of Chen et al.²⁵ to produce a hexagonally close-packed monolayer of 450-nm carboxylated latex spheres (Invitrogen) on glass substrates as a lithographic mask, as described previously.²⁶ The spheres were concentrated from 4% to 20% w/v by centrifugation for the CSA procedure. Monolayers of latex spheres were formed on silicon nitride TEM grids with silicon dioxide support films (Ted Pella) by drop casting 0.5 μL of a diluted (4:1 dilution with DI water) latex sphere suspension onto the TEM grids and allowing them to dry in air, covered. Silver metal (99.999%, International Advanced Materials) was vacuum deposited onto the prepared glass substrates and TEM grids by electron beam evaporation (3-kW electron gun, Thermionics). Glass substrates were cut into approximate 1 × 1 mm squares and attached to 15-mm AFM specimen discs (Ted Pella) with wax. The mask of latex spheres was removed from the glass substrates and the TEM grids by mechanical separation with tape followed by 60-s rinses in ethanol and DI water.

2.3.2 Analytical Techniques

Height data was collected with a NanoScope IIIa Multimode AFM (Veeco) equipped with a J scanner. The AFM was operated in tapping mode in air using silicon probes (Bruker) with nominal spring constants of 20-80 N/m and resonant frequencies of 230-410 kHz. Images were collected with a 512×512 pixel resolution, a $5 \times 5 \mu\text{m}$ scan size, and a 0.5 Hz scan rate. Each image was corrected for baseline tilt using the “Flatten” tool of the NanoScope software, and spurious scan lines were removed with the “Erase Scan Lines” tool. The deconvolution algorithm of Markiewicz and Goh was used assuming a spherical tip of radius 10 nm in order to filter out high frequency noise from the AFM data.²⁷ The “Particle Analysis” extension of the NanoScope software was used for data analysis. Irregularly shaped particles caused by defects in the lithographic mask or by aggregation were excluded from the analysis. Each $5 \times 5 \mu\text{m}$ scan was considered one measurement of the mean Ag NP height. Triplicate measurements were performed for each specimen at each time point. Reported values of mean heights are weighted averages of the triplicate measurements, where the number of particles in a scan area was used as the weighting factor. The average number of particles measured per scan was 128, and the minimum number of particles in a single scan was 30. TEM imaging was performed with an FEI Titan 80-300 field-emission TEM equipped with an EDAX r-TEM detector for energy dispersive X-ray spectroscopy (EDS) measurements or a JEOL 2100 field thermionic emission TEM equipped with a silicon drifted detector-based EDS system. DigitalMicrograph (Gatan) was used to execute fast Fourier transforms (FFT) of TEM images and to measure d-spacings. Scanning electron microscopy (SEM) imaging was performed with an FEI Quanta 600 FEG environmental SEM with a Bruker EDS with a silicon drifted detector. Samples were sputter-coated for 30 s

with gold-palladium before SEM imaging. A standardless Cliff-Lorimer thin foil approximation was used to calculate atomic percentages from EDS spectra.

2.3.3 Sulfidation and Dissolution Laboratory Experiments

ACS grade sodium sulfide nonahydrate (Alfa Aesar) was dissolved in 18.2 M Ω -cm deionized (DI) water (Barnstead) for sulfidation experiments. A 5 mM sodium bicarbonate buffer was added to sulfide solutions to raise the pH to 8.6 or higher to limit the effect of H₂S volatilization. According to our equilibrium calculations using Visual MINTEQ (ver. 3.0), >97% of the dissolved sulfide would be in the form of HS⁻ under these conditions. No buffer was added to the NaCl solutions used for dissolution experiments. During an exposure, all solutions were kept at room temperature (~22 °C) and placed in the dark.

Prior to exposure to Na₂S solutions, specimens were exposed to 100 mM NaCl for 1 d. In our previous work, we found that Ag NPs produced by NSL initially increased in height and decreased in radius upon exposure to NaCl. The in-plane shape also changed from triangular to circular. We used X-ray photoelectron spectroscopy (XPS) to demonstrate that the height increase was not due to the formation of an AgCl layer. Hence, the change appears to be purely morphological rather than chemical, and further discussion of this effect can be found in our previous work.²⁶ Because of the potential this morphological change has to confound AFM measurements of sulfidation by causing a height increase not associated with a change in Ag NP density, the initial NaCl exposure was deemed necessary to allow this height increase to occur before the sulfidation experiments began.

For sulfidation experiments, prepared specimens were placed in 50-mL polypropylene tubes and immersed in 40 mL of Na₂S solutions (0.01-10 μ M) for 2 d. The specimens were characterized by AFM before and after each exposure. TEM grids were placed in 50-mL glass

beakers and immersed in 10 mL of 10 μ M Na₂S for 2 d. For dissolution experiments, specimens that had been exposed to 1 mM Na₂S for 0, 5, 15, or 30 min were placed in 15-mL polystyrene sample tubes (Fisher Scientific) and exposed to 10 mL of 550 mM NaCl. The specimens were removed periodically for AFM measurements and then returned to the NaCl solution.

2.3.4 Field Deployment in a Wastewater Treatment Plant

Specimens were prepared as described above and characterized by AFM to determine their initial mean height. Individual specimens were placed in tissue cassettes (Fisher), and twelve such cassettes were secured inside a 13 × 13 × 4 cm pewter cage. The cage was lined with netting to ensure that materials loosened by mixing would not escape the cage during field deployment. Two of these cages were deployed simultaneously at the Christiansburg, Virginia WWTP on March 24-30 and April 21-30, 2014. During the first deployment, one cage was placed in an anoxic zone of the activated sludge process and the other in an aerated zone. An anoxic zone precedes aerated zones in the activated sludge basins at the Christiansburg WWTP. The anoxic zone is fed by primary effluent and return activated sludge. No nitrate recycle was fed into the anoxic zone at the time of this study. Cages were placed in the primary influent and secondary effluent of the WWTP during the second deployment. During this deployment, a TEM grid holder containing two prepared grids was placed in the cage in the primary influent. The grid holder was covered with filter paper to prevent damage to the grids while permitting adequate exposure to the wastewater. Triplicate specimens were removed from each cage periodically during the course of the experiment for analysis. The specimens were rinsed with ethanol and DI water following removal from the cages, and the ethanol and DI water rinses were repeated once the specimens were returned to the lab. WWTP staff measured temperature, pH, and dissolved oxygen (DO) at about 8 AM daily.

2.4 RESULTS AND DISCUSSION

2.4.1 Laboratory Study of Sulfidation

Prior to field deployment, a detailed laboratory study of Ag NP sulfidation was performed. Five replicate specimens were exposed to 10 μM Na_2S (pH 9.1) for 2 d. Representative images of the Ag NP arrays and the measured height distributions both before and after exposure are shown in Figure 2-1. Significantly, the characteristic NSL pattern was still discernible after the exposure, which suggests that the primary particles were sulfidized directly in place rather than dissolving and precipitating as secondary Ag_2S particles. The mean particle height increased by an average factor (\pm standard deviation) of 1.28 ± 0.01 . Bednar et al. measured an increase in Ag NP diameter from 27 to 35 nm (a factor of 1.30) during a 4-d aqueous exposure to Na_2S ,²⁸ and Chen et al. observed that Ag NP diameters increased by a factor of 1.14 following reaction with gaseous H_2S .²⁹ Due to the difference in the atomic volumes of silver metal and acanthite (the stable mineral form of Ag_2S at geologically low temperatures and pressures), uniform conversion of Ag^0 to acanthite would theoretically increase the linear dimensions of an individual Ag NP by a factor of 1.19.²⁹ The difference between the theoretical and measured value can be explained by a combination of factors. First, the Ag NP height distribution broadened following sulfidation, which indicates that the reaction was not uniform. This result agrees with observations that Ag_2S crystallites form as discontinuous, irregular protrusions from silver surfaces rather than uniform films.^{12, 30, 31} Additionally, Levard et al. found that the Ag_2S formed by sulfidation of Ag NPs typically consisted of roughly two-thirds amorphous material.¹⁶ If amorphous Ag_2S is less dense than acanthite, then the growth factor would be greater than the value calculated from the atomic volume of acanthite. Lastly, several studies report that excess sulfur can be present on the surface of sulfidized Ag NPs in sulfur-rich environments, possibly as elemental sulfur or chemisorbed

sulfides.^{12, 13, 29} The presence of this excess sulfur would also effectively augment the observed increase in Ag NP size.

Additional 2-d exposures at lower Na₂S concentrations (each at pH 8.6) were also performed. The ratio of final mean height to initial mean height was 1.01, 1.00, 1.01, and 1.21 for 0, 0.01, 0.1, and 1 μM Na₂S concentrations, respectively. Of these four conditions, only the 1 μM Na₂S exposure yielded a statistically significant (95% confidence) increase in mean particle height. Because the mean Ag NP height did not decrease significantly in the bicarbonate buffer without Na₂S, we can conclude that oxidative dissolution caused by the buffer solution was negligible during the 2-d sulfidation period used in this study. Ag NP sulfidation reportedly follows first-order kinetics with respect to sulfide concentration.¹² Thus, each tenfold decrease in Na₂S concentration would likewise decrease the sulfidation rate by a factor of ten. Accordingly, the sulfidation reaction may be complete within a day or two in 1 μM sulfide, whereas the reaction may last up to 10 or 20 d in 0.1 μM sulfide. Based on a comparison between Ag NP dissolution and sulfidation kinetics, Liu et al. predicted that sulfidation would occur by a heterogeneous mechanism at sulfide concentrations above ~0.8 μM and by a dissolution/precipitation mechanism at lower sulfide concentrations.¹² Notably, we observed the heterogeneous conversion of Ag NPs to Ag₂S at a sulfide concentration near their predicted crossing point, but not below it. Others found the formation of acanthite bridges between Ag NPs following exposure to Na₂S, which is indicative of a dissolution/precipitation mechanism.¹⁶ In a later report, they noted the presence of core/shell structures and acanthite nanocrystal precipitates in addition to acanthite bridges, and they suggested that the S:Ag molar ratio might play a role in the favored structure.¹⁸ These studies used relatively low S:Ag concentration ratios ranging from 0.02:1 up to 2:1 with sulfide concentrations of 1 and 15 mM.^{16, 18} Based on our previous

characterization of NSL-produced Ag NP arrays,²⁶ we estimate an average mass of $\sim 0.1 \mu\text{g}$ Ag on the specimens used in this study and S:Ag molar ratios of 400:1 and 40:1 for the 10 and 1 μM Na_2S solutions, respectively. Under these conditions, sulfidation is rapid compared to dissolution and the heterogeneous sulfidation mechanism dominates.

TEM was used to gain additional insight into the sulfidation process. Prior to sulfidation, NSL-produced Ag NPs were polycrystalline FCC silver (Appendix A, Figures A-1 and A-2). As shown in Figure 2-2, EDS confirmed that the Ag NPs were converted to Ag_2S during exposure to Na_2S . The numerous smaller nanoparticles seen in Figure 2-2A were produced during the silver deposition process (Appendix A, Figure A-3). It is possible that these small particles obscure the presence of Ag_2S precipitates in the 2-10 nm size range; thus, they prevent us from concluding that no nanoscale secondary precipitates were formed by a dissolution/precipitation mechanism. The Ag:S atomic ratios for EDS spectra taken at the centers of Particles I and II were 1.9 and 2.1, respectively. These results suggest complete conversion to Ag_2S , but an EDS spectrum averaged over the entirety of Particle I yielded a ratio of 2.5. This ratio is high enough to indicate that sulfidation was not complete throughout the entire particle. A closer examination of Particle II with high resolution TEM confirmed that silver metal was still present after the 2-d exposure to 10 μM Na_2S (Figure 2-3). The pronounced Moiré fringes in Figure 2-3B mark the overlap of two adjacent crystals. FFT analysis of the two crystals revealed d-spacings of 2.36, 1.50, and 1.17 Å for Crystal I and 3.10, 2.65, 2.24, 2.08, and 1.96 Å for Crystal II. The measured d-spacings for Crystals I and II closely match those reported for FCC silver ([111], [220], and [222] planes) and acanthite ([111], [120], [031], [200], and [113] planes), respectively.^{29, 32} The dark field TEM image in Figure 2-3A reveals that Crystal II (acanthite) is the dominant phase in Particle II. Similar conclusions can be drawn for Particle I, but a general lack of lattice fringes (and the

corresponding spots in the FFT) suggests that some portions of Particle I may actually be amorphous Ag₂S rather than acanthite (Appendix A, Figure A-4).

Liu et al. inferred from sulfide depletion measurements, which were stoichiometrically consistent with complete sulfidation, that sulfidized Ag NPs would not have a uniform passivating layer of Ag₂S to protect a metallic core from further corrosion.¹² The present investigation demonstrates the non-uniform nature of the sulfidation reaction. A uniform shell of Ag₂S did not form around a core of metallic Ag. Rather, large portions of the Ag NPs were sulfidized, while small portions near the edges were not. The importance of this observation is that sulfidation does not create a passivating layer. Even after near complete sulfidation, some silver metal remains in contact with the solution phase and is available for further sulfidation or oxidation followed by the release of Ag⁺ to the surrounding environment. Others have similarly concluded that sulfidized Ag NPs can have a complex crystal structure where Ag metal may remain near the surface where it is available for dissolution.¹⁵ It is possible that the anisotropic shape of Ag NPs produced by NSL led to the non-uniformity of the reaction through enhanced sulfidation of the edges and corners of the particles. In this case, quasi-spherical particles, the most likely shape of Ag NPs to enter the environment, might be expected to form a more uniform corrosion layer during sulfidation; however, quasi-spherical Ag NPs are frequently polycrystalline,^{33, 34} which could provide a similar opportunity for sulfidation to begin at high energy sites and continue in a non-uniform pattern through the rest of the nanoparticle.^{15, 35}

To evaluate the effects of sulfidation on Ag NP dissolution rates, three specimens were exposed to 1 mM Na₂S (pH 10.0) for 5, 15, and 30 min and increased in height by factors of 1.00, 1.07, and 1.16, respectively. These three specimens and one unsulfidized specimen were then placed in 550 mM NaCl solutions (pH 6.0) and removed periodically for AFM height

analysis over the course of 2 wk. We showed in our previous work that concentrated NaCl solutions are highly corrosive to Ag NPs, and a detailed discussion about the effects of chloride on Ag NP dissolution rates can be found therein.²⁶ Dissolved silver primarily forms soluble chloride complexes (AgCl_2^- and AgCl_3^{2-}) under these conditions.¹¹ The experimental results are summarized in Figure 2-4. The dissolution rates progressively decreased as sulfidation time increased, which illustrates that Ag_2S is more resistant to oxidation and dissolution than silver metal under these conditions. It is not surprising that the 5 and 15 min exposures did not completely prevent Ag NP dissolution. As mentioned previously, sulfidation did not produce a uniform film around the Ag NPs; therefore, partial sulfidation leaves a portion of the Ag NP surface in contact with the solution and permits continued dissolution, albeit at a reduced rate due to partial conversion to the more stable Ag_2S phase. The dissolution rate for the specimen with the longest sulfidation time was not significantly different than zero; thus, a sufficient degree of sulfidation can effectively halt Ag^+ release. We note that this specimen was also only partially sulfidized, so it is probable that dissolution did not entirely cease in this case but was not measurable by our technique over the 2-wk dissolution period.

Our results corroborate previous findings. The observation that the degree of sulfidation affects the degree of growth inhibition of *E. coli* agrees with our observations that partially sulfidized Ag NPs still dissolve and that the sulfidation process is not uniform.¹⁸ Levard et al. reported a decrease in Ag^+ release rates following Ag NP exposure to Na_2S , and the extent of the decrease depended on the degree of sulfidation; however, they also observed a high degree of aggregation in their system.¹⁶ Aggregation following sulfidation was noted by others as well,¹² and it may in part result from the displacement of the Ag NPs' stabilizing surface coating by sulfide.^{16, 36, 37} Because aggregation can reduce nanomaterial dissolution rates,³⁸⁻⁴⁰ this competing

process can confound experiments that attempt to examine the dissolution of Ag_2S relative to the initial Ag NPs. Our experimental technique eliminates aggregation; thus, our findings explicitly demonstrate that sulfidized Ag NPs are more resistant to oxidative dissolution than pristine Ag NPs under the conditions of this study.

Our final lab experiment was to expose Ag NPs to raw sewage sludge from the Christiansburg WWTP to determine if our technique could be used to measure sulfidation even in complex environmental samples. Details of the exposure are included in the SI. The NSL pattern remained intact throughout the 6-d exposure (Appendix A, Figure A-5), which highlights the ability of our technique to probe nanomaterial transformations in complex media. Both AFM (Appendix A, Figure A-6) and TEM (Appendix A, Figure A-7) indicated that the Ag NPs had been partially sulfidized during the exposure. Again, the primary Ag NPs were sulfidized directly and the reaction was not uniform. Following exposure to sludge, Ag NPs did not dissolve significantly in 500 mM NaCl (Appendix A, Figure A-6B). The presence of an organic film on the Ag NPs led us to hypothesize that organic matter could hinder the sulfidation process. As a simple test of this hypothesis, we performed sulfidation experiments in the presence of 100 μM citrate, 100 μM bovine serum albumin, and 25 mg/L humic acid (International Humic Substances Society, Suwannee River Humic Acid Standard II). The change in Ag NP height over a 2-d exposure was not significantly different in the experimental samples than it was in the positive control (i.e., solutions of 10 μM Na_2S without added organic molecules). Ag NP heights decreased slightly in negative controls (i.e., solutions with organic molecules but no added sulfide). These results do not provide support for the hypothesis that organic matter decreases Ag NP sulfidation rates.

2.4.2 Field Deployment in a Wastewater Treatment Plant

During the deployment in anoxic and aerated zones of the activated sludge basin, the average (\pm standard deviation in each case) water temperature was 12.5 ± 0.7 °C, the average pH was 6.9 ± 0.1 , and the average volume percent of solids in the mixed liquor was 84%. In the aerated zone, the average DO was 2.6 ± 2.3 mg/L. During the second set of experiments, the average influent and effluent temperature were 13.7 ± 0.7 °C and 15.3 ± 0.6 °C, respectively, and the average influent and effluent pH were 7.5 ± 0.1 and 7.2 ± 0.1 , respectively. The DO of the secondary effluent measured on April 3, 2014 was 1.2 mg/L. Although the DO of the mixed liquor leaving the aeration basin was only 0.5 mg/L, substantial aeration due to mixing at a flow splitter led to a DO level of 1.4 mg/L entering the secondary clarifier. The DO of the primary influent was not measured, but it was assumed to be extremely low due to the high organic content and lack of aeration. The average flow rate in the WWTP at the time of the experiments was 2.4 MGD, and the average return activated sludge flow rate was 1.7 MGD. The average solids retention time (SRT) was 10 d. Experiments performed in a pilot-scale WWTP demonstrated that Ag NPs associate strongly with biosolids in wastewater;¹⁴ therefore, SRT may be considered a characteristic residence time of Ag NPs in a WWTP. For this reason, our field experiments were carried out for 7-10 d. Of course, Ag NPs would not be exposed to primary influent or secondary effluent for this length of time, but a similar time period was used for both field deployments so that the results would be comparable.

We were again able to track the primary Ag NPs by AFM, which suggests that the primary particles were converted directly to Ag₂S in the WWTP as they had been in our laboratory study. The change in Ag NP height in the different zones of the WWTP is shown in Figure 2-5. Ag NPs in both the anoxic zone and the primary influent significantly increased in height while no

significant change in height occurred in the aerobic zone or the secondary effluent. This result suggests that sulfidation occurs almost exclusively in anaerobic zones of the WWTP, in agreement with previous batch studies.¹⁴ Recent work has shown that copper sulfide and zinc sulfide can react with Ag NPs to form Ag₂S even under oxic conditions, but our results do not provide evidence of this reported mechanism in aerobic zones of the Christiansburg WWTP.³⁵ An oxidation step must take place for sulfidation of Ag NPs to occur, and it is evident that oxygen is not the oxidant in our field study. It has been shown that in the presence of sulfides some quinones and nitro compounds can oxidize Ag NPs,⁴¹ hence, certain organic constituents of the wastewater may act as the electron acceptor for the sulfidation reaction. This conclusion suggests that the use of oxysulfidation kinetics for prediction of Ag NP sulfidation rates in the environment may be of limited utility.¹²

The sulfidation kinetics in the anoxic zone and primary influent were very similar. The initial sulfidation rates were determined by performing linear regression on the data points representing the first 4 d of exposure. Assuming that sulfidation is complete once the height has increased by a factor of 1.3 and that the sulfidation reaction is uniform, the initial sulfidation rates were 11-14 nm Ag converted to Ag₂S per day. At this rate, the Ag NPs used in this study would be completely sulfidized within 5 d. In both cases, the mean height had increased by a factor of 1.3 by 7 d. In the primary influent, the height had increased by a factor of 1.35 after 9 d. This increase corresponds approximately to an additional 4 nm. Adsorbed organic matter may account for this extra 4 nm. In the aerobic zone and the secondary effluent, a small initial increase in height of about 2-3 nm appears to have occurred. Although this result is not statistically significant, it is consistent with the notion that an organic film several nanometers thick formed on the Ag NPs during their exposure to wastewater.

SEM/EDS confirmed that the changes observed by AFM were due to sulfidation. The background signal of the glass substrate was much stronger than the signal from the Ag NPs, so EDS spectra had to be obtained from small aggregates and large, irregular particles instead of individual Ag NPs (Appendix A, Figure A-8). The average Ag:S ratios from specimens that had been in the anoxic zone and primary influent for 7-10 d were 1.2 and 0.91, respectively. These averages are subject to substantial errors because the silver and sulfur signals were quite weak relative to the background, but they clearly indicate a high degree of sulfidation. In contrast, the average Ag:S ratio of a specimen that had been in the secondary effluent for 10 d was 42.

TEM was used to further probe sulfidation of Ag NPs that had been in the primary influent for ~10 d. TEM images are shown in Figure 2-6. FFT analysis of high resolution TEM images revealed d-spacings of 2.85, 2.67, 2.25, 2.05, 2.00, and 1.95 Å, all of which match expected d-spacings for acanthite.³² EDS line scans were taken across each Ag NP in Figure 2-6A, and the average Ag:S ratio was 2.3, indicating near complete sulfidation. The ratio remained nearly constant along the cross section of each particle. By this point in the sulfidation process, little variability remained in the chemical composition from one point to another on a particle. Not surprisingly, an intense C peak appeared in all the EDS spectra from the line scans. Wastewater has a high organic content, and some of this organic material is likely to adsorb to the Ag NPs, probably through thiol linkages, and to the SiO₂ support film. A ~3-nm thick layer of amorphous, low molecular weight material is apparent near the edge of the Ag NP in Figure 2-6B. This thin layer could consist of the adsorbed organic material responsible for the intense C peak. The presence of an organic film that is several nanometers thick is consistent with our conclusion that adsorption of organic matter contributed to the height increase observed by AFM.

2.4.3 Environmental Implications

By using microscopic techniques to track the characteristic pattern of Ag NPs fabricated on glass slides and TEM grids by NSL, we have clearly demonstrated that primary Ag NPs are directly converted to Ag_2S in anaerobic regions of a full-scale WWTP. The Ag NPs maintained their original positions and, to a large extent, their original shapes even after complete or near complete conversion to Ag_2S . The magnitude of the height increase due to sulfidation suggests that little, if any, Ag^+ was lost to the solution. Our results demonstrate that Ag NPs do not first dissolve and then form secondary Ag_2S particles, or that this mechanism is negligible in wastewater, because if such a mechanism were dominant the Ag NPs would have decreased in height rather than increased in height. Previous work inferred such a heterogeneous reaction through indirect measurements of Ag NP sulfidation,¹² but the present study provides direct confirmation of the theorized mechanism. Other microscopic investigations found evidence of a dissolution/precipitation mechanism of sulfidation, but these studies were carried out at silver and sulfide concentrations that were different from what would be expected in real-world environments.^{16, 18} It is still possible that a dissolution/precipitation step does occur in which sulfide catalyzes dissolution and the original particle is the preferred site for precipitation. For example, isotope tracer studies have shown that goethite nanorods maintain their size, shape, and phase even after extensive exchange between aqueous and goethite iron phases.⁴² However, if such a dissolution step does occur in our system, it must be followed immediately by a precipitation step so that the dissolved species cannot diffuse into solution and become bioavailable or form secondary precipitates apart from the primary particles; otherwise, Ag NPs deployed in the WWTP would not have grown by a factor as large as the particles in our laboratory studies. The importance of this conclusion is that toxic Ag^+ ions will not be released

from Ag NPs as an intermediate species prior to the formation of Ag₂S as they pass through wastewater infrastructure.¹² Furthermore, we have shown that sulfidized Ag NPs are more resistant to oxidation and dissolution than pristine Ag NPs, even in the absence of aggregation induced by sulfidation. Hence, sulfidation will prevent disturbances of biological wastewater treatment processes and mitigate potential harm to ecosystems in the receiving waters. However, another notable conclusion of this research is that sulfidation does not proceed uniformly, so the potential for silver dissolution and toxicity is not completely eliminated until sulfidation is complete. Indeed, partially sulfidized Ag NPs did dissolve under our experimental conditions, albeit at a slower rate than pristine Ag NPs.

It is significant that we were able to gain detailed information about changes in the morphology, crystallinity, and chemical composition of Ag NPs during field deployment in a full-scale WWTP. We were also able to measure the sulfidation kinetics of Ag NPs in different regions of the WWTP. The success of our method in these regards demonstrates that immobilizing nanomaterials on substrates is a useful technique for studying nanomaterial fate and transformations in the environment and adds to the recent success of similar field studies performed in natural water bodies.²² This technique overcomes challenges posed by the unrealistically high nanomaterial concentrations and overly simplistic test media that plague many studies of the environmental implications of nanotechnology.

REFERENCES

1. Marambio-Jones, C.; Hoek, E. M. V. A review of the antibacterial effects of silver nanomaterials and potential implications for human health and the environment. *J. Nanopart. Res.* **2010**, *12*, 1531-1551.
2. Morones, J. R.; Elechiguerra, J. L.; Camacho, A.; Holt, K.; Kouri, J. B.; Ramirez, J. T.; Yacaman, M. J. The bactericidal effect of silver nanoparticles. *Nanotechnology* **2005**, *16*, 2346-2353.
3. Sondi, I.; Salopek-Sondi, B. Silver nanoparticles as antimicrobial agent: A case study on *E. coli* as a model for gram-negative bacteria. *J. Colloid Interface Sci.* **2004**, *275*, 177-182.
4. Benn, T. M.; Westerhoff, P. Nanoparticle silver released into water from commercially available sock fabrics. *Environ. Sci. Technol.* **2008**, *42*, 4133-4139.
5. Geranio, L.; Heuberger, M.; Nowack, B. The behavior of silver nanotextiles during washing. *Environ. Sci. Technol.* **2009**, *43*, 8113-8118.
6. Gottschalk, F.; Sonderer, T.; Scholz, R. W.; Nowack, B. Modeled environmental concentrations of engineered nanomaterials (TiO₂, ZnO, Ag, CNT, fullerenes) for different regions. *Environ. Sci. Technol.* **2009**, *43*, 9216-9222.
7. Fabrega, J.; Luoma, S. N.; Tyler, C. R.; Galloway, T. S.; Lead, J. R. Silver nanoparticles: Behaviour and effects in the aquatic environment. *Environ. Int.* **2011**, *37*, 517-531.
8. Xiu, Z. M.; Ma, J.; Alvarez, P. J. J. Differential effect of common ligands and molecular oxygen on antimicrobial activity of silver nanoparticles versus silver ions. *Environ. Sci. Technol.* **2011**, *45*, 9003-9008.
9. Lok, C. N.; Ho, C. M.; Chen, R.; He, Q. Y.; Yu, W. Y.; Sun, H.; Tam, P. K. H.; Chiu, J. F.; Che, C. M. Silver nanoparticles: Partial oxidation and antibacterial activities. *J. Biol. Inorg. Chem.* **2007**, *12*, 527-534.
10. Yin, L.; Cheng, Y.; Espinasse, B.; Colman, B. P.; Auffan, M.; Wiesner, M.; Rose, J.; Liu, J.; Bernhardt, E. S. More than the ions: The effects of silver nanoparticles on *Lolium multiflorum*. *Environ. Sci. Technol.* **2011**, *45*, 2360-2367.
11. Levard, C.; Hotze, E. M.; Lowry, G. V.; Brown, G. E. Environmental transformations of silver nanoparticles: Impact on stability and toxicity. *Environ. Sci. Technol.* **2012**, *46*, 6900-6914.
12. Liu, J. Y.; Pennell, K. G.; Hurt, R. H. Kinetics and mechanisms of nanosilver oxysulfidation. *Environ. Sci. Technol.* **2011**, *45*, 7345-7353.
13. Kim, B.; Park, C. S.; Murayama, M.; Hochella, M. F. Discovery and characterization of silver sulfide nanoparticles in final sewage sludge products. *Environ. Sci. Technol.* **2010**, *44*, 7509-7514.
14. Kaegi, R.; Voegelin, A.; Sinnet, B.; Zuleeg, S.; Hagendorfer, H.; Burkhardt, M.; Siegrist, H. Behavior of metallic silver nanoparticles in a pilot wastewater treatment plant. *Environ. Sci. Technol.* **2011**, *45*, 3902-3908.
15. Kaegi, R.; Voegelin, A.; Ort, C.; Sinnet, B.; Thalmann, B.; Krismer, J.; Hagendorfer, H.; Elumelu, M.; Mueller, E. Fate and transformation of silver nanoparticles in urban wastewater systems. *Water Res.* **2013**, *47*, 3866-3877.
16. Levard, C.; Reinsch, B. C.; Michel, F. M.; Oumahi, C.; Lowry, G. V.; Brown, G. E. Sulfidation processes of PVP-coated silver nanoparticles in aqueous solution: Impact on dissolution rate. *Environ. Sci. Technol.* **2011**, *45*, 5260-5266.

17. Lombi, E.; Donner, E.; Taheri, S.; Tavakkoli, E.; Jamting, A. K.; McClure, S.; Naidu, R.; Miller, B. W.; Scheckel, K. G.; Vasilev, K. Transformation of four silver/silver chloride nanoparticles during anaerobic treatment of wastewater and post-processing of sewage sludge. *Environ. Pollut.* **2013**, *176*, 193-197.
18. Reinsch, B. C.; Levard, C.; Li, Z.; Ma, R.; Wise, A.; Gregory, K. B.; Brown, G. E.; Lowry, G. V. Sulfidation of silver nanoparticles decreases *Escherichia coli* growth inhibition. *Environ. Sci. Technol.* **2012**, *46*, 6992-7000.
19. Choi, O.; Cleuenger, T. E.; Deng, B. L.; Surampalli, R. Y.; Ross, L.; Hu, Z. Q. Role of sulfide and ligand strength in controlling nanosilver toxicity. *Water Res.* **2009**, *43*, 1879-1886.
20. Blaser, S. A.; Scheringer, M.; MacLeod, M.; Hungerbuhler, K. Estimation of cumulative aquatic exposure and risk due to silver: Contribution of nano-functionalized plastics and textiles. *Sci. Total Environ.* **2008**, *390*, 396-409.
21. Dobias, J.; Bernier-Latmani, R. Silver release from silver nanoparticles in natural waters. *Environ. Sci. Technol.* **2013**, *47*, 4140-4146.
22. Sekine, R.; Khaksar, M.; Brunetti, G.; Donner, E.; Scheckel, K. G.; Lombi, E.; Vasilev, K. Surface immobilization of engineered nanomaterials for in situ study of their environmental transformations and fate. *Environ. Sci. Technol.* **2013**, *47*, 9308-9316.
23. Haynes, C. L.; Van Duyne, R. P. Nanosphere lithography: A versatile nanofabrication tool for studies of size-dependent nanoparticle optics. *J. Phys. Chem. B* **2001**, *105*, 5599-5611.
24. Hulteen, J. C.; Vanduyne, R. P. Nanosphere lithography: A materials general fabrication process for periodic particle array surfaces. *J. Vac. Sci. Technol. A-Vac. Surf. Films* **1995**, *13*, 1553-1558.
25. Chen, K.; Stoianov, S. V.; Bangerter, J.; Robinson, H. D. Restricted meniscus convective self-assembly. *J. Colloid Interface Sci.* **2010**, *344*, 315-320.
26. Kent, R. D.; Vikesland, P. J. Controlled evaluation of silver nanoparticle dissolution using atomic force microscopy. *Environ. Sci. Technol.* **2011**, *46*, 6977-6984.
27. Markiewicz, P.; Goh, M. C. Atomic-force microscopy probe tip visualization and improvement of images using a simple deconvolution procedure. *Langmuir* **1994**, *10*, 5-7.
28. Bednar, A. J.; Poda, A. R.; Mitrano, D. M.; Kennedy, A. J.; Gray, E. P.; Ranville, J. F.; Hayes, C. A.; Crocker, F. H.; Steevens, J. A. Comparison of on-line detectors for field flow fractionation analysis of nanomaterials. *Talanta* **2012**, *104*, 140 - 148.
29. Chen, R.; Nuhfer, N. T.; Moussa, L.; Morris, H. R.; Whitmore, P. M. Silver sulfide nanoparticle assembly obtained by reacting an assembled silver nanoparticle template with hydrogen sulfide gas. *Nanotechnology* **2008**, *19*.
30. Elechiguerra, J. L.; Larios-Lopez, L.; Liu, C.; Garcia-Gutierrez, D.; Camacho-Bragado, A.; Yacamán, M. J. Corrosion at the nanoscale: The case of silver nanowires and nanoparticles. *Chem. Mater.* **2005**, *17*, 6042-6052.
31. Liu, J. Y.; Sonshine, D. A.; Shervani, S.; Hurt, R. H. Controlled release of biologically active silver from nanosilver surfaces. *ACS Nano* **2010**, *4*, 6903-6913.
32. Downs, R. T. In *The RRUFF project: An integrated study of the chemistry, crystallography, Raman and infrared spectroscopy of minerals*, Program and Abstracts of the 19th General Meeting of the International Mineralogical Association, Kobe, Japan, July 23-28, 2006; International Mineralogical Association: Kobe, Japan, 2006.
33. Wiley, B.; Herricks, T.; Sun, Y. G.; Xia, Y. N. Polyol synthesis of silver nanoparticles: Use of chloride and oxygen to promote the formation of single-crystal, truncated cubes and tetrahedrons. *Nano Lett.* **2004**, *4*, 1733-1739.

34. Zhang, W.; Yao, Y.; Sullivan, N.; Chen, Y. S. Modeling the primary size effects of citrate-coated silver nanoparticles on their ion release kinetics. *Environ. Sci. Technol.* **2011**, *45*, 4422-4428.
35. Thalmann, B.; Voegelin, A.; Sinnet, B.; Morgenroth, E.; Kaegi, R. Sulfidation kinetics of silver nanoparticles reacted with metal sulfides. *Environ. Sci. Technol.* **2014**, *48*, 4885-4892.
36. Strelow, F.; Henglein, A. Time-resolved chemisorption of I⁻ and SH⁻ on colloidal silver particles (a stopped-flow study). *J. Phys. Chem.* **1995**, *99*, 11834-11838.
37. Linnert, T.; Mulvaney, P.; Henglein, A. Surface-chemistry of colloidal silver: Surface-plasmon damping by chemisorbed I⁻, SH⁻, and C₆H₅S. *J. Phys. Chem.* **1993**, *97*, 679-682.
38. Liu, J.; Aruguete, D. M.; Murayama, M.; Hochella, M. F. Influence of size and aggregation on the reactivity of an environmentally and industrially relevant nanomaterial (PbS). *Environ. Sci. Technol.* **2009**, *43*, 8178-8183.
39. Rubasinghege, G.; Lentz, R. W.; Park, H.; Scherer, M. M.; Grassian, V. H. Nanorod dissolution quenched in the aggregated state. *Langmuir* **2010**, *26*, 1524-1527.
40. Gondikas, A. P.; Morris, A.; Reinsch, B. C.; Marinakos, S. M.; Lowry, G. V.; Hsu-Kim, H. Cysteine-induced modifications of zero-valent silver nanomaterials: Implications for particle surface chemistry, aggregation, dissolution, and silver speciation. *Environ. Sci. Technol.* **2012**, *46*, 7037-7045.
41. Henglein, A.; Mulvaney, P.; Linnert, T. Chemistry of Ag_n aggregates in aqueous-solution: Nonmetallic oligomeric clusters and metallic particles. *Faraday Discuss.* **1991**, *92*, 31-44.
42. Handler, R. M.; Beard, B. L.; Johnson, C. M.; Scherer, M. M. Atom exchange between aqueous Fe(II) and goethite: An Fe isotope tracer study. *Environ. Sci. Technol.* **2009**, *43*, 1102-1107.

FIGURES

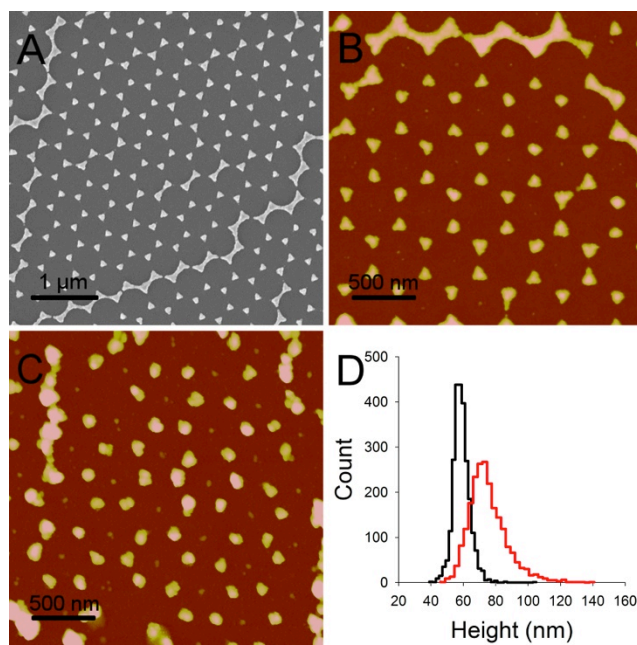


Figure 2-1. A) SEM and B) AFM images of unsulfidized Ag NP arrays produced by NSL. C) AFM image of an Ag NP array after a 2-d exposure to 10 μM Na₂S. D) Ag NP height distributions before (black) and after (red) the exposure.

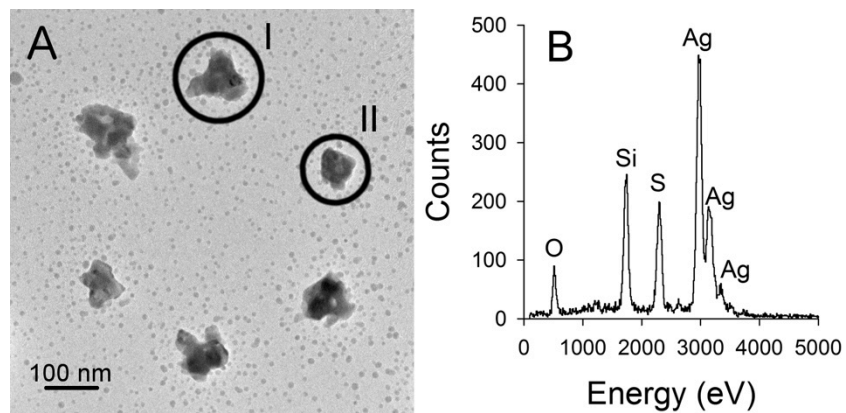


Figure 2-2. A) Bright field TEM image of NSL-produced Ag NPs after a 2-d exposure to 10 μ M sodium sulfide. Particles I and II are indicated in the circles. B) EDS spectrum from Particle I.

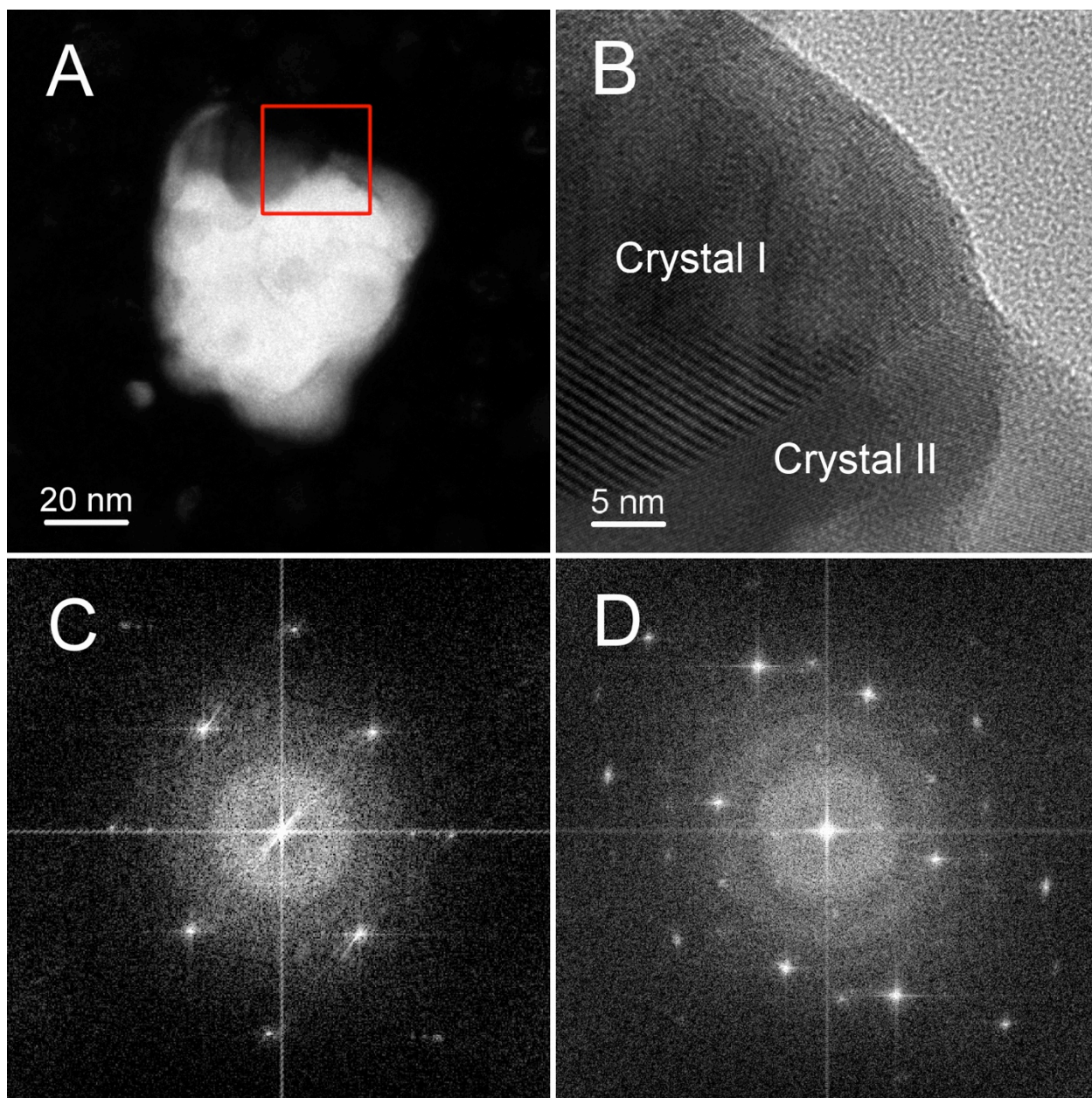


Figure 2-3. A) Dark field TEM image of Particle II (see Figure 2-2A). B) High resolution TEM image of the area marked in A. FFTs from C) Crystal I and D) Crystal II.

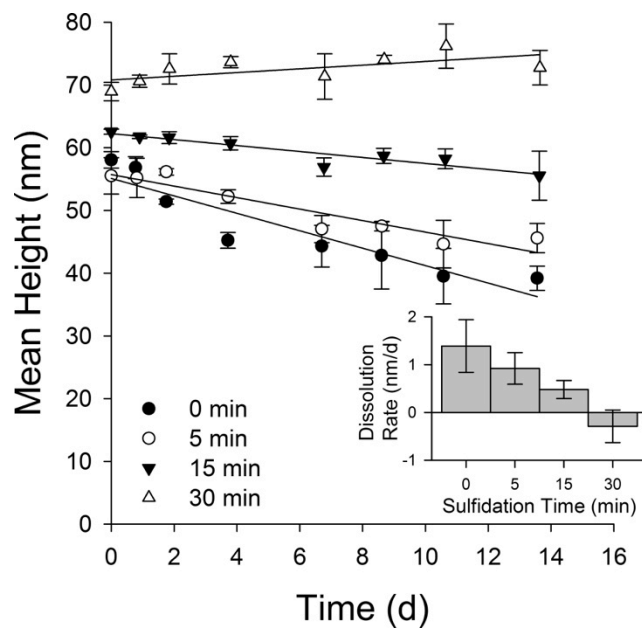


Figure 2-4. Mean height measured by AFM over time for Ag NPs exposed to 550 mM NaCl (pH 6.0). Prior to exposure to the NaCl solution, particles were exposed to 1 mM Na₂S for 0, 5, 15, or 30 min. Error bars represent standard deviations of triplicate measurements. Inset: Dissolution rates calculated by linear regression for the different sulfidation times. Error bars indicate 95% confidence intervals.

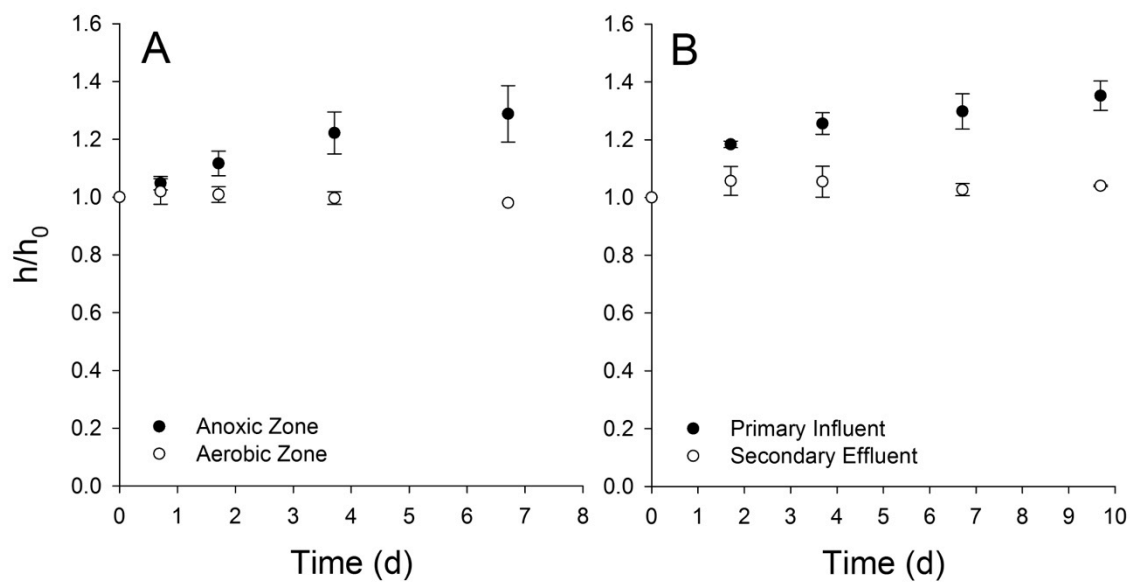


Figure 2-5. Ratio of mean height (h) to initial mean height (h_0) measured over time by AFM for Ag NP arrays deployed in A) anoxic and aerobic zones of an activated sludge basin on March 24-30, 2014 and B) primary and secondary clarifiers on April 21-30, 2014. Error bars represent standard deviations of triplicate samples.

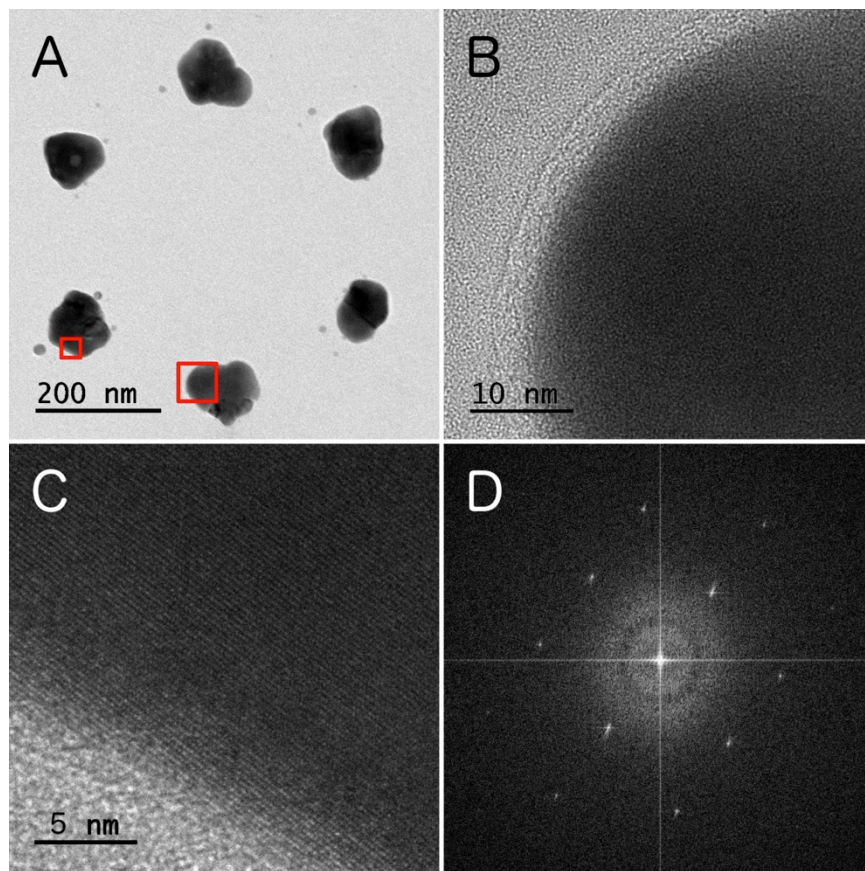


Figure 2-6. A) Bright field TEM image of NSL-produced Ag NPs after a 10-d exposure in the primary influent of the Christiansburg WWTP. B) High resolution TEM image of the region marked by the larger square in A. C) High resolution TEM image of the region marked by the smaller square in A. D) FFT of the image in C.

3 Dissolution and Persistence of Copper-Based Nanomaterials in Unsaturated Solutions

3.1 ABSTRACT

Copper-based nanoparticles (NPs) are becoming increasingly common in commercial products. Release of these materials into the environment raises concerns about the potentially unique risks they pose to aquatic life. Successful prediction of environmental concentrations of Cu-based NPs requires an understanding of their chemical transformations and persistence. In this study, nanosphere lithography was used to fabricate immobilized Cu-based NPs on glass substrates. Metallic copper, cupric oxide/hydroxide, and copper sulfide NPs were investigated. Dissolution rate constants for a contracting volume rate law were directly measured *in situ* over a pH range of 4.8-11.3. Changes in Cu-based NP size were monitored by an atomic force microscope equipped with a flow-through cell. The flowing solution remained unsaturated with respect to cupric solid phases by continually flushing dissolved Cu ions out of the flow cell. Based on the measured rate constants, CuO/Cu(OH)₂ NPs are expected to dissolve completely within a matter of hours, even at neutral to basic pH. The expected persistence of metallic Cu NPs ranges from a few hours to days, depending on the pH. Cu_xS NPs were more persistent, showing no significant dissolution over the time scales studied. Field deployment of Cu-based NP samples in a freshwater stream confirmed these conclusions for a natural aquatic system.

3.2 INTRODUCTION

Increased production of Cu-based nanoparticles (NPs) has raised concerns over the unintended impacts these materials might have on the environment.¹⁻³ Cu-based NPs have their most direct route to natural aquatic systems through their application as pesticides in agriculture

and as antifouling paints applied to boat hulls.^{1,4,5} The novel properties of nanomaterials can result in unique ecotoxicological impacts that are distinct from the well known toxic effects of dissolved Cu ions.^{6,7} Indeed, several studies have found evidence that Cu-based NPs exert direct toxic effects apart from the toxicity due to ion release and represent a risk to aquatic organisms.^{2,8-11}

Assessing the risks of Cu-based NPs requires an understanding of their exposure routes and environmental transformations. Transformations of interest include oxidation, sulfidation, and dissolution. Metallic Cu NPs can become oxidized as they age to form cuprous or cupric phases.¹² Various oxidized minerals are present in Cu-based anti-microbial products,⁴ and these Cu minerals may be converted to Cu_xS NPs (where x can take on many values for stable sulfide minerals at room temperature, including 1, 1.12, 1.39, 1.6, 1.75, 1.8, 1.95, and 2) following transport to anaerobic regions such as aquatic sediments.¹³⁻¹⁵ Any of these forms of Cu-based NPs can dissolve and release cuprous and cupric ions into solution. An important question is how long Cu-based NPs will persist in their nanoparticulate form once they enter the environment. If dissolution is rapid, then Cu-based NPs represent nothing more than an additional input of a well known environmental contaminant—dissolved copper ions. On the other hand, Cu-based NPs may present an additional novel risk if they are environmentally persistent.

Previous research investigating the environmental implications of Cu-based NPs has generally reported limited dissolution above neutral pH values.^{1,2,8,10,11,13,14,16-18} The initial NP concentrations in these studies range from 0.01-200 mg/L, with 10 mg/L being typical, and the solutions quickly become saturated with cupric ions. These concentrations may be representative of transient Cu-based NP loadings in agricultural runoff following a storm event, but average nanomaterial concentrations in the environment are predicted to be in the ng/L to $\mu\text{g/L}$ range.¹⁹⁻²¹

Keller and Lazareva estimated that the concentration of Cu-based NPs entering the San Francisco Bay through wastewater discharge would be <100 ng/L, with a lower bound near 0.1 ng/L.²¹ By way of comparison, the median background level of dissolved copper in uncontaminated freshwaters is 3 µg/L.^{22,23} The abundance of natural ligands in aquatic systems ensures that most of the dissolved Cu fraction is present as complexes, primarily associated with the chelating functional groups of natural organic matter (NOM).^{5,23,24} The formation of these complexes shifts the Cu equilibrium toward the dissolved phase.^{14,25,26} Consequently, Cu-based NPs entering the environment will often find themselves in unsaturated solutions, and the concentrations of Cu-based NPs will be too dilute to saturate these waters. In spite of the environmental relevance of such dilute solutions, few studies have examined dissolution of Cu-based NPs in solutions that remain unsaturated with respect to cupric solid phases throughout the experiment.

Another common feature of previous studies of the environmental fate and toxicity of Cu-based NPs is that the NPs are highly aggregated.^{11,16,18,27} Nanomaterial aggregation is generally modeled as a second-order reaction with respect to particle number, so the homoaggregation rate may be quite low in natural systems where nanomaterial concentrations are dilute; heteroaggregation is expected to play a more important role in the environment.²⁸ Aggregation can substantially diminish nanomaterial reactivity and dissolution by effectively decreasing the available surface area and by hindering mass transport of reactants within dense aggregate structures.²⁹⁻³³ This decrease in reactivity and increase in size due to aggregation can reduce NP toxicity;^{34,35} thus, unaggregated NPs may exert a toxic effect disproportionately to their number concentration relative to aggregates.

To quantify the dissolution and persistence of Cu-based NPs in unsaturated solutions, we employed a continuous flow setup with an atomic force microscopy (AFM) system. The continuously flowing solution flushed dissolved ions from the AFM fluid cell so that unsaturated conditions were maintained. Metallic Cu NPs were prepared by nanosphere lithography (NSL).³⁶ This high-throughput technique produces uniform arrays of immobilized NPs on glass substrates to prevent detachment and aggregation during dissolution experiments.³⁷ NSL-produced Cu NPs were pre-treated with ozone and sulfide to produce CuO/Cu(OH)₂ and Cu_xS NPs, and the dissolution rates of all three types of NPs were measured. The prepared specimens are field deployable,³⁸ and we used this ability to investigate the dissolution of Cu-based NPs in a natural freshwater stream.

3.3 MATERIALS AND METHODS

3.3.1 Sample Preparation

Cover glass substrates (Fisher) were cleaned by immersion in an aqueous solution of 4% NH₄OH/16% H₂O₂ at 75 °C for 10 min followed by immersion in 14% HCl/14% H₂O₂ at 75 °C for 10 min (caution: the solutions used in this cleaning procedure are corrosive). The substrates were rinsed thoroughly with deionized (DI) water (18.2 MΩ-cm, Barnstead) after each cleaning step and stored in DI water until further use. Hexagonally close-packed monolayers of 450-nm carboxylated latex spheres (Life Technologies) were deposited onto cleaned substrates by convective self-assembly according to the procedure of Chen et al., as described previously.^{37,39} Prior to the deposition, the latex spheres were concentrated from 4% to 20% w/v by centrifugation. The monolayer of spheres acts as a lithographic mask during the subsequent metal deposition. Metals were vacuum deposited onto the substrates by electron beam evaporation (3-kW electron gun, Thermionics). About 10 nm of titanium (99.995%, International

Advanced Materials) was deposited on the prepared substrates prior to deposition of copper (99.999%, International Advanced Materials). Ti improves the adhesion between Cu and the glass substrate to limit Cu NP detachment due to shear stresses under the flowing conditions in the AFM fluid cell. Ti is quite chemically stable relative to Cu, so its influence on the oxidation kinetics during dissolution experiments should be negligible. Immediately prior to use, the substrates were cut to a size of $\sim 1 \text{ mm}^2$ and attached to 15-mm stainless steel AFM specimen discs (Ted Pella) with wax. The latex spheres were removed with tape and subsequent rinses for 30 s in ethanol and DI water.

3.3.2 Ozone and Sulfide Treatments

Specimens were oxidized by ozone for 10-15 min to convert Cu NPs to CuO/Cu(OH)_2 NPs. Ozone was generated by flowing 5 L/min of filtered air through an Enaly EOZ-300Y ozone generator. The ozone concentration measured by a 49C ozone analyzer (Thermo) was 80 mg/L. The flow rate was measured with a mini-Buck calibrator (A. P. Buck, Inc.). Specimens were sulfidized by placing them in solutions of 100 μM ACS grade sodium sulfide nonahydrate (Alfa Aesar) + 5 mM NaHCO_3 (pH 9.6) for 3 d. Greater than 99% of sulfide is in the form of HS^- at this pH. Sulfidation proceeded at room temperature (22 °C).

3.3.3 Sample Characterization

Scanning electron microscopy (SEM) images were taken with a LEO (Zeiss) 1550 Schottky field-emission SEM. Specimens were sputter coated with gold-palladium for 30 s prior to SEM imaging. Scanning transmission electron microscopy (STEM) analysis was performed with a JEOL 2100 field thermionic emission TEM equipped with a silicon drift detector-based energy dispersive X-ray spectroscopy (EDS) system. Dark field imaging utilized an annular detector. Selected area electron diffraction (SAED) patterns were analyzed by the circular Hough

transform technique in DigitalMicrograph (Gatan). A PHI Quantera X-ray photoelectron spectroscopy (XPS) microprobe was used for collecting XPS spectra. Peak fitting of XPS spectra was performed with CasaXPS, and spectra were adjusted to the adventitious carbon peak at 284.6 eV. The average mass of Cu per unit area of substrate was measured by dissolving the Cu from 10 replicate specimens in 10 mL of 5% HNO₃ overnight followed by analysis by inductively coupled plasma mass spectrometry (ICP-MS). The acid was diluted in DI water from 67-70% trace metals grade HNO₃ (Fisher). Digital photographs were taken of the specimens prior to the digestion to measure the area of each substrate using ImageJ (NIH).

3.3.4 Dissolution Experiments

Height measurements were performed with a NanoScope IIIa Multimode AFM (Bruker) equipped with a J scanner. The AFM was operated in tapping mode in a flow-through setup with a glass fluid cell and silicon nitride probes (0.58 N/m nominal spring constant). The root-mean-squared amplitude of the freely oscillating cantilever was maintained between 0.5-1.0 V. Images were captured with a scan rate of 0.5 Hz, a 3 μm scan size, and a 256 \times 256 resolution. For these scan parameters, a single scan lasts 8.5 min; however, each measurement was taken to be a single point in time midway through the scan. A 50 μm x -offset was set to avoid the so-called tip-shielding effect while the AFM was not scanning. The AFM was equilibrated for 1-2 h prior to each experiment to reduce drift, with the exception of experiments where dissolution was too rapid to allow time for equilibration (*i.e.*, Cu NPs at pH 4.8 and CuO/Cu(OH)₂ NPs at pH 5.6 and 6.6). The sample was loaded and the solution was flowing during this equilibration period. Drift in the x - y plane during the experiments was less than 1 μm . A scan was performed about every 30-60 min over a period of 1-6 h so that 2-8 scans were performed per experimental run. The “Flatten” tool of the NanoScope software was used to correct baseline tilt of the acquired images,

and the “Erase Scan Lines” tool was used to remove spurious scan lines. The mean height was obtained from each AFM image with the “Particle Analysis” extension of the NanoScope software. Irregularly shaped nanostructures and aggregates were excluded from the analysis. Rate constants were obtained directly from the slope of a linear regression on the time series height data. Reported rate constants are the mean from at least triplicate tests for each experimental condition. DI water was used for all dissolution experiments. The pH was adjusted above 5.6 with 0.2 N NaOH (Crescent Chemical Company) and below 5.6 with ACS-grade acetic acid (Fisher). Solutions adjusted with NaOH were mixed and allowed to equilibrate with atmospheric CO₂ overnight. Water was drawn from a glass container through the AFM fluid cell by a syringe pump (Model 500D, Teledyne Isco) at a rate of 2 mL/min. The water temperature in the glass container was 22 °C. The temperature is elevated in the fluid cell due to the laser light and mechanical oscillations; however, the relatively short detention time (3 s) should ensure that the temperature in the liquid cell is near the temperature of the entering water.

3.3.5 Field Deployment

Specimens were deployed in Stroubles Creek in Blacksburg, Virginia on May 9, 2015 from 10:00 AM to 9:30 PM. Two pewter cages, each containing 18 specimens fastened individually within tissue cassettes (Fisher), were suspended in the creek with steel cables. Triplicate specimens of Cu, CuO/Cu(OH)₂, or Cu_xS NPs were removed from a cage at each time point. Upon removal from the creek, specimens were immersed for 30 s in DI water adjusted to pH 11.3 by NaOH to remove dissolved salts. Excess water was wicked away with Kimwipes (Kimberly-Clark). AFM measurements were performed before and after the field deployment to determine the change in mean height for each specimen. Height measurements were performed by tapping-mode AFM in air with silicon probes (Bruker) with nominal spring constants of 20-

80 N/m and resonant frequencies of 230-410 kHz. The scan parameters for these measurements were a scan rate of 0.5 Hz, a 5 μm scan size, and a 512×512 resolution. Three scans were performed per replicate, so a total of 9 scans were performed for each nanomaterial at each time point. A portable pH, temperature, and TDS meter was used to measure these water quality parameters throughout the day. Water depth was measured directly, and surface velocity was estimated by measuring the time taken for debris on the water surface to travel a known distance. Three 40 mL water samples were taken from the creek at morning, midday, and night for TOC analysis. The samples were returned to the lab and stored at 4 °C overnight prior to analysis with a Shimadzu TOC-VCP by combustion catalytic oxidation with a non-dispersive infrared detector.

3.4 RESULTS AND DISCUSSION

The overall oxidation and dissolution reactions for Cu, Cu₂O, CuO, Cu₂S, and CuS are given in Equations 3-1 through 3-6.



The reactions are intentionally written proceeding only in the forward direction because of our claim that our system is far from equilibrium. Accordingly, the products will have a negligible effect on the reaction rates. Dissolved oxygen and pH are expected to play an important role in the dissolution reactions, with reaction rates increasing as pH decreases and as dissolved oxygen

increases. We note that the system is much more complex than is implied by Equations 3-1 through 3-6. Various oxide, hydroxide, and carbonate complexes and solid phases, crystalline or amorphous, may form during the dissolution process. The distribution of these species will vary with pH, and the chemical composition of the NP surface may have an important effect on the observed dissolution rate. Moreover, reactive oxygen intermediates might form during the oxidative dissolution of Cu and Cu_xS NPs.^{40,41} The speciation and reactivity of these intermediates might also vary with pH. Additional dissolved species include carbonate and hydroxide complexes. Elucidating the mechanistic pathway for these reactions is beyond the scope of the present work. Rather, the empirically observed reaction rates for the dissolution of the Cu-based NPs at varying pH were determined.

3.4.1 Dissolution Kinetics Model

Nanomaterial dissolution studies often use first-order kinetic models where the dissolution rate is assumed to be proportional to the remaining mass in the system;^{25,40} however, nanomaterial dissolution is a surface-mediated reaction, so not all the mass in the system is available for reaction at a given time. Therefore, it is more reasonable to assume that the reaction rate is proportional to the available surface area. This relationship is expressed by the contracting volume rate law given in Equation 3-7:

$$\frac{dV}{dt} = -kA \quad (3-7)$$

where dV/dt is the first derivative of particle volume with respect to time, A is the reactive surface area, and k is a rate constant with units of length divided by time.⁴² We have assumed that the reaction is far from equilibrium; otherwise, Equation 3-7 would include an additional term for the reverse reaction that would depend on the solution concentration of the dissolved

species. The rate constant in Equation 3-7 is pseudo-first order because it hides the dependence of the reaction rate on pH and dissolved oxygen, which both remain approximately constant during our experiments.

Dividing both sides of Equation 1 by molar volume, V_m , and rearranging, we get Equation 3-8:

$$\frac{1}{A} \frac{dN}{dt} = -\frac{k}{V_m} \quad (3-8)$$

where dN/dt is the rate at which moles of metal ion are being lost from a particle, so the units on either side of the equation are moles per unit area per unit time. Equation 3-8 shows that the mass-based dissolution rate normalized by surface area is constant; thus, k can be obtained by solution phase concentration measurements. In practice, Equation 3-8 is difficult to use because of the uncertainty of surface area measurements, especially if the nanoparticles are aggregating during the dissolution measurements so that A is changing in an unpredictable fashion. Gondikas *et al.* demonstrated this difficulty in their research on silver nanoparticle dissolution. They reported that the initial dissolution rate normalized by geometrical surface area was significantly lower for fast aggregating particles compared with slowly aggregating particles.⁴³ Assuming that the surface area remains constant at its geometrical maximum while the effective surface area is in fact decreasing due to aggregation would lead one to calculate an apparent rate constant by Equation 3-8 that is smaller in magnitude than the true rate constant.

If the dissolving particles are assumed to be spherical, then the surface area term drops out entirely and Equation 3-7 simplifies to the contracting sphere rate law:

$$\frac{dr}{dt} = -k \quad (3-9)$$

where dr/dt is the rate of change of the spherical particle's radius, r . According to Equation 3-9, the rate of change of r is constant and gives a direct measure of k . Nanoparticles produced by NSL are not spherical; they are truncated tetrahedra. The triangular corners dissolve more rapidly than other regions of the particles because of the high surface energy associated with the corners' sharp curvature; thus, Equation 3-9 does not apply initially. However, because the corners dissolve rapidly, the initial shape is transient, and the particles are converted to nanodisks.^{37,44,45} As derived in Appendix B, Equation 3-9 holds for cylindrical particles if we assume that the rate of change of height is equal to the rate of change of the radius. Based on our previous work with silver, this assumption is quite reasonable,³⁷ so Equation 3-9 is valid in our system after the initial shape transition. The time series data reported herein and in our previous work show that the height of dissolving NSL-produced nanoparticles decrease at a constant rate, as predicted by Equation 3-9.^{37,38} Once k has been determined, the particle lifetime can be calculated by Equation 3-10:

$$\tau_L = \frac{d_0}{2k} \quad (3-10)$$

where τ_L is the lifetime of the particle with units of time, and d_0 is the initial diameter of the particle. Particle lifetime is a useful concept for understanding the environmental persistence of dissolving particles, analogous to the way half-life has been used for a range of contaminants. For example, if a particle has an initial diameter of 100 nm and k is 1 nm/h in a particular environment, then the particle will dissolve completely after 50 h in that environment.

For a single particle or a perfectly monodisperse suspension, the concentration of dissolved copper ions, $[Cu^{2+}]$, at time t for a batch process is given by Equation 3-11:

$$[Cu^{z+}] = [Cu^{z+}]_0 \left[1 - \left(1 - \frac{t}{\tau_L} \right)^3 \right] \quad (3-11)$$

where $[Cu^{z+}]_0$ is the initial mass of metal expressed as an equivalent concentration. For a polydisperse suspension, $[Cu^{z+}]$ is determined by taking the summation of each individual particle's contribution. More practically, the dispersion can be divided into several size fractions, each with a characteristic initial diameter. The contribution from each size fraction is calculated using Equation 3-11, and then the summation of all contributions is calculated to obtain the total $[Cu^{z+}]$. Equation 3-11 is only valid for $0 \leq t \leq \tau_L$. For $t > \tau_L$, the particles have completely dissolved and do not release any more ions. It should be noted that Equations 3-9, 3-10, and 3-11 assume that the spherical particles are not aggregating, but remain singly dispersed throughout the dissolution period. Thus, for aggregating suspensions, Equation 3-10 sets a lower limit for particle lifetime and Equation 3-11 sets an upper limit on the metal ion concentration at time t .

Finally, Equation 3-12 gives the mass balance on metal ions for the flow cell used in this study:

$$\frac{d[Cu^{z+}]}{dt} = \frac{3[Cu^{z+}]_0}{\tau_L} \left(1 - \frac{t}{\tau_L} \right)^2 - \frac{[Cu^{z+}]}{\tau_R} \quad (3-12)$$

where τ_R is the residence time in the flow cell, and the other variables are as defined previously. The first term on the right side of the equation is the rate of generation of Cu ions due to particle dissolution, and it is obtained by differentiating Equation 3-11 with respect to time. The second term on the right side of the equation represents the loss due to dissolved ions exiting the fluid cell. The solution to Equation 3-12 is given in Appendix B. This model assumes that the particles are hemispheres, that there is complete mixing within the flow cell, and that all the mass in the

system consists of nanoparticles with a perfectly uniform size distribution. These assumptions are further discussed below.

3.4.2 Nanomaterial Characterization

Cu NPs produced by NSL initially had a bright yellow glow observable under a 10× microscope. Following treatment with ozone or sulfide this glow was replaced with a black color, indicating that the original Cu NPs had chemically reacted with the ozone and sulfide. SEM micrographs and AFM height distributions of Cu, CuO/Cu(OH)₂, and Cu_xS NPs are shown in Figure 3-1. The chemical treatments notably altered the initial nanomaterial morphology. The median heights measured for Cu, CuO/Cu(OH)₂, and Cu_xS NPs were 68.9, 86.8, and 94.2 nm, respectively. After accounting for the presence of a 10.8 nm titanium film underlying the nanoparticles (see Materials and Methods section for details), the original Cu NPs increased by a factor of 1.31 and 1.44 following oxidation and sulfidation, respectively. Based on differences in atomic volume, the linear dimensions of Cu NPs would increase by factors of 1.03, 1.21, 1.52, 1.25, and 1.42 after a uniform conversion to Cu₂O (cuprite), CuO (tenorite), Cu(OH)₂ (spertiniite), Cu₂S (chalcocite), and CuS (covellite), respectively. A comparison of these predicted values with the measured values suggests that tenorite and covellite are the most likely phases produced by the oxidation and sulfidation reactions; however, this inference is far from conclusive because the conversion was not uniform. The initial Cu NPs had a rather uniform size distribution with a standard deviation of only 2.8 nm, but the standard deviation increased to 8.3 nm following sulfidation and to 12.4 nm following ozonation. The calculation also assumes complete conversion from metallic copper to the new solid phase. In the dissolution experiments discussed in the subsequent section, the dissolution rate remained constant throughout the dissolution period for the majority of the ozonated Cu NPs; therefore, the NPs apparently had

been completely oxidized so that no metallic core remained. There were only a couple instances in which a core-shell structure was evidenced by a distinct shift of the dissolution rate (Appendix B, Figure B-1).

The total mass of copper per unit area of substrate was found to be 143 ± 37 ng/mm² (values are expressed as mean \pm standard deviation unless otherwise noted). The average area of a single substrate was 1.3 ± 0.4 mm², so the average mass per specimen was 186 ± 70 ng. This mass is greater than what would be expected for a substrate that was only covered by the nanoparticles of interest, which would only be about 48 ng, or 26% of the actual mass.³⁷ For comparison, a copper thin film of equivalent thickness covering the entire substrate would have a mass of 677 ng. The difference between the measured and calculated mass of Cu NPs is due to defects in the initial lithographic mask of latex spheres. Irregular nanostructures caused by line defects in the mask can be seen in the SEM images of Figure 3-1. These nanostructures cover substrate area that would not be covered by the individual NPs. Other features on the substrates include Cu thin films where no latex spheres had been deposited and areas with no Cu whatsoever where a multilayer of spheres had been deposited. Because the Cu NPs cannot occupy the same substrate area as any of these defects, the nanoparticles themselves actually contribute significantly less than 26% to the total mass. This fact will be important for interpreting the system under study.

The chemical composition and crystal structure of the nanomaterials was investigated by STEM/EDS (Figure 3-2). EDS maps illustrate that oxygen was strongly associated with copper following ozonation, and sulfur was strongly associated with copper following sulfidation. It also appears that a minor amount of oxygen was associated with the pristine Cu NPs; however, this could be an artifact attributable to the thickness of the particles. The measured atomic percentage

of O in the Cu NP samples was only $3 \pm 2\%$, and some fraction of this percentage is due to background oxygen rather than oxygen in the structure of the Cu NPs. In contrast, the atomic percentage Cu:O ratio in the ozonated samples was 0.9 ± 0.1 for the particles shown in Figure 3-2D, which is very near the 1:1 ratio expected for CuO. On the other hand, the Cu:O ratio measured from a similar set of nanoparticles on a separate TEM sample was 0.4 ± 0.1 , which is closer to the 1:2 ratio expected for $\text{Cu}(\text{OH})_2$. The average Cu:S ratio of the nanoparticles shown in Figure 3-2G was 1.4 ± 0.3 , and the ratio ranged from 1.0 to 2.4. The ratio matches spionkopite ($\text{Cu}_{1.39}\text{S}$) well, but the high variability suggests that multiple Cu_xS phases were present.

The brightest spots in the SAED patterns shown in Figure 3-2A and 3-2D are due to the underlying silicon substrate. These spots do not appear in the Cu_xS samples, which were prepared on glass instead. The diffraction spots due to the particles themselves show up as rings in all three types of Cu-based NPs due to the polycrystalline nature of the particles. The d-spacings determined by SAED for Cu NPs were 2.09, 1.83, 1.27, and 1.09 Å, in good agreement with the reported values for the [111], [200], [220], and [311] crystal faces of metallic face-centered cubic Cu.⁴⁶ The two bright rings in the SAED pattern for the ozonated NPs are due to the two most intensely diffracting crystal faces of tenorite—the [-111] and [111] faces with measured d-spacings of 2.51 and 2.32 Å, respectively. The [110], [202], and [-113] faces of tenorite were also detected, with respective d-spacings of 2.75, 1.58, and 1.50 Å.⁴⁶ In contrast, the region where the Cu:O ratio was 0.4 had d-spacings of 2.78, 2.64, 2.48, 2.24, 2.07, and 1.77 Å. The two most intense peaks of tenorite were absent, and the remaining peaks closely match the [110], [002], [111], [130], [131], and [060] faces of spertiniite. The SAED results corroborate the EDS data to confirm the presence of both tenorite and spertiniite in the ozonated samples. Thus, these samples contain a mixture of CuO and $\text{Cu}(\text{OH})_2$ NPs. This result is consistent with

the broad height distribution observed by AFM following ozonation and the fact that the median height increased by a factor intermediate between what would be expected for tenorite and spertiniite. The SAED results for Cu_xS NPs also demonstrate a mixture of phases. Measured d-spacings of 3.09, 2.87, 2.77, and 1.93 Å match both spionkopite and yarrowite ($\text{Cu}_{1.12}\text{S}$). On the other hand, measured d-spacings of 3.30 and 3.23 Å match the [100] and [101] faces of covellite.⁴⁶ Ma *et al.* likewise found that sulfidation of Cu-based NPs results in a milieu of stable copper sulfide phases.

These STEM analyses are not sensitive to the chemical composition at the surface of the particles, so XPS, which is sensitive only to a 1-10 nm depth within the sample, was used to investigate surface composition (Figure 3-3). Curve fitting to the Cu $2p_{3/2}$ peak of Cu NPs found a primary peak at 932.7 eV and a shoulder at 933.8 eV. The primary peak is due to metallic copper, and the shoulder indicates the presence of cupric oxide.^{12,47} The presence of cupric species is also evident from the characteristic shake-up bands that appear at 943 and 962 eV.^{12,47} These results suggest that the Cu NPs have a thin cupric oxide shell around the metallic core. The much more pronounced shake-up bands of the CuO/Cu(OH)_2 NPs at 942.0 and 944.2 eV demonstrate that the ozonation process had strongly oxidized the surface so that cupric species became dominant. A strong peak at 934.9 eV demonstrates that cupric hydroxides were the dominant surface species following ozonation. Unfortunately, the distribution between oxides and hydroxides could not be further elucidated by investigation of the O 1s region because of the overwhelming oxygen signal from the glass substrate. Finally, the main Cu $2p_{3/2}$ peak had shifted to 932.4 eV for the Cu_xS NPs, consistent with a conversion to the cuprous oxidation state present in copper sulfides such as chalcocite and covellite.⁴⁸ Weak shake-up satellites and a shoulder at 933.7 eV demonstrate that some cupric species are also present. The S 2p doublet at 162.1 and

163.3 eV is attributable to copper sulfide species.⁴⁸ The additional doublet at 168.4 eV is a clear sign that exposure to the atmosphere had caused oxidation to sulfate, which may also be why the Cu(II) oxidation state is present in the Cu 2p region. Thus, a thin layer of copper sulfate appears to coexist with the more abundant cuprous sulfide species. The C 1s region revealed that adventitious carbon and carbonates were present on the surface of all samples, so cupric carbonates may account for some of the oxidized Cu observed in all the samples (Appendix B, Figure B-2).

3.4.3 Nanomaterial Dissolution

Representative AFM images and height time series from the continuous flow dissolution experiments are shown in Figures 3-4 and 3-5, respectively. It is qualitatively evident from these figures that dissolution was rapid for CuO/Cu(OH)₂ NPs, negligible for Cu_xS NPs, and intermediate for Cu NPs. Linear regression did not show statistically significant dissolution for any of the Cu_xS replicates at any pH. Wang *et al.* likewise observed a decrease in the dissolution rate of CuO NPs following sulfidation,¹⁴ and this diminished dissolution rate is consistent with the effects of sulfidation on other metals, including Ag and Zn.^{38,49,50} On the other hand, Ma *et al.* observed an apparent increase in dissolution of CuO NPs following sulfidation. This increase was primarily attributed to the presence of copper sulfates and poorly ordered phases with higher solubility as well as the formation of small CuS clusters that were counted as part of the dissolved fraction because of their ability to pass through filters; however, some of the dissolution was due to oxidation of Cu_xS species to form soluble copper sulfates.¹³ The oxidative dissolution of copper sulfides observed in that study took place over a dissolution period of >10 d, much longer than the 6 h dissolution periods used in the present work. It has also been shown that Cu_xS present in fresh biosolids become less abundant after 6-24 months of stockpiling,

presumably due to oxidation of the reduced sulfur, which stands in contrast with Ag_2S that was found to be stable in biosolids even after 6 months of stockpiling.^{51,52} The significance of these results is that Cu and CuO/Cu(OH)_2 NPs that migrate to anaerobic sediments or enter wastewater streams may become converted to Cu_xS NPs and become environmentally persistent particles that only oxidize slowly over a period of weeks to months in aerobic environments. Although Cu_xS NPs are more persistent than other Cu-based NPs, metal sulfides are generally less reactive and bioavailable; thus, sulfidation is likely to reduce the ecotoxicity of Cu-based NPs.⁵³⁻⁵⁵

The dissolution measurements for Cu_xS NPs agreed with our expectations based on the available literature, but the results for Cu and especially CuO/Cu(OH)_2 NPs were not anticipated. Dissolution rate constants and particle lifetimes at varying pH values for these two nanomaterials are plotted in Figure 3-6. Rate constants decreased with increasing pH and varied from 14.3 to 0.4 nm/h for Cu NPs over the pH 4.8-11.3 range and varied from 30.1 to 1.5 nm/h over the pH 5.6-11.3 range for CuO/Cu(OH)_2 NPs. Lifetimes were calculated over the 0-100 nm size range, which is often the size range in which materials are classified as “nano”.⁷ The results show that CuO/Cu(OH)_2 NPs will dissolve completely within a matter of hours over a pH range that varies from acidic to basic pH. Even the largest CuO/Cu(OH)_2 NPs at pH 11.3 are expected to dissolve completely in less than 2 d. Cu NPs likewise are expected to dissolve over the course of hours in acidic conditions, and up to several days or a week at circumneutral to basic pH. The smallest Cu and CuO/Cu(OH)_2 particles, which are also the most toxic and bioavailable,^{34,56,57} are predicted to dissolve in less than a day at any pH. These results stand in contrast to previous reports of limited dissolution of Cu-based NPs suspended in neutral to basic pH solutions.^{1,2,8,10,11,13,14,16-18} An important difference between this work and previous research is that the continuous flow setup employed herein maintains an unsaturated solution at all times (see the following section for

more details). The relatively high nanomaterial concentrations used in other work results in rapid saturation with respect to highly insoluble oxidized copper phases. Several studies did use concentrations approaching the environmentally relevant range (10 $\mu\text{g Cu/L}$), but these experiments were performed in high ionic strength media (*i.e.*, seawater) where aggregation was rapid and extensive.^{10,11,16} A brief survey of these literature results creates the impression that Cu-based NPs will be persistent in the environment because of their low solubility; however, the condition of unaggregated Cu-based NPs in unsaturated solutions has been neglected until now in spite of its environmental importance. Hence, the present work highlights the pitfall of extrapolating conclusions based on the high concentrations of many experiments to the low concentrations that will actually prevail in the environment.

3.4.4 Estimated Concentrations

The kinetic model used in this study assumes that the system is far from equilibrium so that the dissolved Cu species do not influence the reaction rate. To test this assumption, the dissolved Cu concentration within the AFM fluid cell was estimated. Because the dissolved copper concentrations leaving the fluid cell were dilute, directly measuring the concentration was not attempted. Instead, the dissolved concentration was estimated by the mass balance model given in Equation 3-6. To represent worst-case conditions, we assumed the initial Cu mass was 2 standard deviations above the average mass. The model assumes that complete mixing occurs within the flow cell, which is not correct because of the complex flow pattern caused by the presence of the oscillating cantilever. The AFM cantilever is connected to a base that covered at least 5-10% of the sample during each experiment. Because the flow was restricted underneath the cantilever base, we observed that little or no dissolution occurred in the covered region. The initial mass parameter was reduced slightly to 300 ng to account for this effect. The model

further assumes that the particles are hemispherical, so that the average height is equal to the radius. As discussed above, the initial Cu NPs have triangular corners that dissolve rapidly and the particles are converted to a cylindrical shape. Ignoring the rapid dissolution at the corners underestimates the actual copper release during the initial 1-2 h of the experiment, but the difference between a cylindrical shape and a hemispherical shape is negligible (see Appendix B for discussion). The model also assumes that all the dissolved Cu is in the divalent state. Some small fraction of the dissolved species will actually be cuprous ions, so this assumption overestimates the actual amount of dissolved cupric ion.¹⁸ The most glaring assumption of the model is that the substrate is covered by a uniform distribution of NPs. Less than 26% of the mass on the substrates is from the Cu-based NPs of interest. The rest of the mass is from Cu thin films and irregular nanostructures that resulted from defects in the lithographic mask. These structures have a lower surface area to mass ratio than the NPs; therefore, they release dissolved ions at a slower rate than the NPs and the model output represents an upper bound for the actual dissolved concentration. A lower bound can be estimated by assuming the other extreme; namely, that all the Cu mass is present as a thin film. This assumption results in an estimate that is about a factor of 3 smaller than the model assumption (see Appendix B for details).

Output from the mass balance model is shown in Appendix B, Figure B-3. Because the particle lifetime is much greater than the residence time, the maximum dissolved ion concentration is reached almost instantaneously, and then the ion concentration decreases smoothly until it is zero at about $t = \tau_L$. This decrease becomes more gradual at higher pH values. The initial maximum dissolved concentration was compared with the solubility limit of the least soluble phase (tenorite) for each pH tested (Appendix B, Table B-1). The calculated concentrations are at least one order of magnitude, usually several, below the saturation value in

every case except for CuO NPs at pH 8.4. For this case, the calculated concentration is 756 ng/L, and the solubility limit is 705 ng/L; however, when equilibrium with atmospheric CO₂ is included in the equilibrium calculation the solubility limit increases to 5185 ng/L because of the formation of soluble carbonate complexes. Even in this case the total dissolved Cu is estimated to be much lower than the saturation level. Because the modeled concentrations represent an upper bound, we conclude that the solution is indeed unsaturated. Furthermore, if equilibrium were a controlling factor in the observed dissolution rates in this study, then the rate constants measured at pH 11.3 would have been greater than those measured at pH 8.4 due to the higher solubility at pH 11.3. In contrast, the rate constants for both Cu and CuO/Cu(OH)₂ NPs were lower at pH 11.3 than at pH 8.4. These arguments demonstrate that the assumption that the system is far from equilibrium is justified.

3.4.5 Field Deployment in a Freshwater Creek

The laboratory experiments reported herein used simplistic solutions that are not representative of the natural environment. Aquatic systems have dissolved ions, heterogeneous NOM, natural colloids, and diverse biological activity that were all absent from the experimental solutions employed. It is possible that some constituent of natural waters would chemically stabilize Cu-based NPs and prevent dissolution. To test this possibility, prepared specimens were deployed in Stroubles Creek near Blacksburg, Virginia. The pH in the stream was nearly constant at 7.7 throughout the day, and the temperature varied from 17.2 to 19.0 °C. TDS was 187 ± 13 mg/L, and TOC was 1.31 ± 0.06 mg C/L. The stream depth was 50 cm, and the NP specimens were submerged 5-25 cm below the water surface. Surface velocity of the stream was ~15 cm/s.

Results from the field deployment are shown in Figure 3-7. Although only 5 data points are shown per time series in the figure, it should be noted that each data point represents a total of 9 measurements (36 measurements for the initial point), which imparts a high level of statistical power to the regression analyses. The 95% confidence intervals for the measured values of k are 0.16 ± 0.07 , 27.8 ± 2.2 , and 0.17 ± 0.34 nm/h for Cu, CuO/Cu(OH)₂, and Cu_xS NPs, respectively. Although the measured rate constants for Cu and Cu_xS NPs were nearly the same, the Cu_xS NPs demonstrated much higher sample variability. Due to the high sample variability, the rate constant was not significantly different than zero ($p = 0.33$), and we cannot determine if any dissolution occurred for the Cu_xS NPs. On the other hand, the Cu NP specimens exhibited extremely low variability and the rate constant was highly significant ($p = 5 \times 10^{-5}$). Similarly, the rate constant for CuO/Cu(OH)₂ NPs was significant with $p < 2 \times 10^{-16}$. Based on the results from the laboratory experiments, the Cu NP dissolution was somewhat slower and the CuO/Cu(OH)₂ NP dissolution was much more rapid than was expected. At pH 7.7, the rate constant for Cu NP dissolution should be ~ 0.8 nm/h, more than four times the measured value. The lower temperature in the stream relative to the AFM fluid cell is an important variable that would account for much of the observed difference. The action of NOM could also explain the discrepancy. It has been shown that NOM decreases the oxidative dissolution rate of Ag NPs.⁴⁰ One proposed mechanism for this effect is that the formation of an organic coating layer prevents further oxidation of the NP surface by blocking reactive sites. Alternatively, the NOM may scavenge reactive oxygen intermediates generated during the oxidative dissolution reaction and prevent them from further oxidizing the NP surface.^{40,41} In the case of CuO/Cu(OH)₂ NPs, the predicted rate constant at pH 7.7 is ~ 8.5 nm/h, more than a factor of 3 less than the measured rate. In fact, the value of k measured in Stroubles Creek is close to the value measured at pH 5.6

in the AFM fluid cell experiments. Particles with diameters of 20 and 100 nm would dissolve completely in about 20 min and 2 h at this rate, respectively. Whatever caused this major increase in the rate constant must also have offset the temperature effect that would tend to decrease the dissolution rate relative to the lab measurements. One possibility is that the flow regime in the creek improved transport of reactants to the NP surfaces and increased dissolution by decreasing transport limitations. Another possibility is that dissolved inorganic ions or NOM aggressively complexed the surface-bound oxidized Cu species and facilitated rapid dissolution. Reports in the literature on the effect of NOM on Cu-based NP dissolution are mixed.^{14,18,25,27} Further experimentation is necessary to determine the effects of the different constituents of the creek water. Overall, the field deployment qualitatively confirmed the major conclusions of the lab study.

3.5 CONCLUSIONS

Copper oxides are regarded as insoluble at circumneutral pH as a general rule of thumb. Application of this rule to Cu-based NPs would lead to the conclusion that CuO/Cu(OH)₂ NPs will be persistent in the natural environment. Earlier research has tended to confirm this conventional wisdom; however, these previous studies have investigated Cu-based NPs in systems that either approach the solubility limit of dissolved Cu or exhibit extensive aggregation. Herein, we have shown that unaggregated CuO/Cu(OH)₂ NPs are not environmentally persistent in unsaturated solutions due to rapid dissolution, even at neutral to basic pH. This conclusion was confirmed in a freshwater stream at pH 7.7, where the results suggest that CuO/Cu(OH)₂ NP lifetimes could range from several minutes to 2 h. CuO/Cu(OH)₂ NPs are probably the most abundant Cu-based NPs to enter the environment from commercial products;^{4,12,14} therefore, the finding of their limited persistence in a real aquatic environment has important implications for

the ongoing discussion about metallic nanomaterials as environmental contaminants. In contrast, Cu_xS NPs did not dissolve measurably over the time scales of this study. Cu-based NPs that are sulfidized in anaerobic environments will become much more persistent than the pristine NPs, but they are also expected to become less reactive and less toxic. Cu NPs dissolved at a rate intermediate between $\text{CuO}/\text{Cu}(\text{OH})_2$ and Cu_xS NPs. The results of the field study demonstrated that Cu NPs would dissolve completely after several days to a couple weeks. This time period is relatively short, so Cu NPs are unlikely to accumulate in aquatic environments; however, their lifetime is long enough for the NPs to undergo alternative transformations and interact with aquatic organisms. Because the aggregation process was eliminated for the NPs in this research, the question remains of how aggregation and dissolution will interact to determine the fate of Cu-based NPs in the environment. If aggregation is rapid, then $\text{CuO}/\text{Cu}(\text{OH})_2$ NPs could be spared from dissolution by finding protection within the structure of a dense aggregate. Nevertheless, the smallest and most colloidally stable NPs are perhaps the most bioavailable and toxic, yet these NPs are also the least persistent.

REFERENCES

1. Lin, S. J.; Taylor, A. A.; Ji, Z. X.; Chang, C. H.; Kinsinger, N. M.; Ueng, W.; Walker, S. L.; Nel, A. E. Understanding the Transformation, Speciation, and Hazard Potential of Copper Particles in a Model Septic Tank System Using Zebrafish to Monitor the Effluent. *ACS Nano* **2015**, *9*, 2038-2048.
2. Griffitt, R. J.; Weil, R.; Hyndman, K. A.; Denslow, N. D.; Powers, K.; Taylor, D.; Barber, D. S. Exposure to Copper Nanoparticles Causes Gill Injury and Acute Lethality in Zebrafish (*Danio Rerio*). *Environ. Sci. Technol.* **2007**, *41*, 8178-8186.
3. Hong, J.; Rico, C. M.; Zhao, L. J.; Adeleye, A. S.; Keller, A. A.; Peralta-Videa, J. R.; Gardea-Torresdey, J. L. Toxic Effects of Copper-Based Nanoparticles or Compounds to Lettuce (*Lactuca Sativa*) and Alfalfa (*Medicago Sativa*). *Environmental Science-Processes & Impacts* **2015**, *17*, 177-185.
4. Tegenaw, A.; Tolaymat, T.; Al-Abed, S.; El Badawy, A.; Luxton, T.; Sorial, G.; Genaidy, A. Characterization and Potential Environmental Implications of Select Cu-Based Fungicides and Bactericides Employed in US Markets. *Environ. Sci. Technol.* **2015**, *49*, 1294-1302.
5. Kiaune, L.; Singhasemanon, N., Pesticidal Copper (I) Oxide: Environmental Fate and Aquatic Toxicity. In *Reviews of Environmental Contamination and Toxicology, Vol 213*, Whitacre, D. M., Ed. Springer: New York, 2011; Vol. 213, pp 1-26.
6. Nel, A.; Xia, T.; Madler, L.; Li, N. Toxic Potential of Materials at the Nanolevel. *Science* **2006**, *311*, 622-627.
7. Klaine, S. J.; Alvarez, P. J. J.; Batley, G. E.; Fernandes, T. F.; Handy, R. D.; Lyon, D. Y.; Mahendra, S.; McLaughlin, M. J.; Lead, J. R. Nanomaterials in the Environment: Behavior, Fate, Bioavailability, and Effects. *Environ. Toxicol. Chem.* **2008**, *27*, 1825-1851.
8. Griffitt, R. J.; Luo, J.; Gao, J.; Bonzongo, J. C.; Barber, D. S. Effects of Particle Composition and Species on Toxicity of Metallic Nanomaterials in Aquatic Organisms. *Environ. Toxicol. Chem.* **2008**, *27*, 1972-1978.
9. Shaw, B. J.; Al-Bairuty, G.; Handy, R. D. Effects of Waterborne Copper Nanoparticles and Copper Sulphate on Rainbow Trout, (*Oncorhynchus Mykiss*): Physiology and Accumulation. *Aquatic Toxicology* **2012**, *116*, 90-101.
10. Gomes, T.; Pinheiro, J. P.; Cancio, I.; Pereira, C. G.; Cardoso, C.; Bebianno, M. J. Effects of Copper Nanoparticles Exposure in the Mussel *Mytilus Galloprovincialis*. *Environ. Sci. Technol.* **2011**, *45*, 9356-9362.
11. Buffet, P. E.; Richard, M.; Caupos, F.; Vergnoux, A.; Perrein-Ettajani, H.; Luna-Acosta, A.; Akcha, F.; Amiard, J. C.; Amiard-Triquet, C.; Guibbolini, M., et al. A Mesocosm Study of Fate and Effects of CuO Nanoparticles on Endobenthic Species (*Scrobicularia Plana*, *Hediste Diversicolor*). *Environ. Sci. Technol.* **2013**, *47*, 1620-1628.
12. Mudunkotuwa, I. A.; Pettibone, J. M.; Grassian, V. H. Environmental Implications of Nanoparticle Aging in the Processing and Fate of Copper-Based Nanomaterials. *Environ. Sci. Technol.* **2012**, *46*, 7001-7010.
13. Ma, R.; Stegemeier, J.; Levard, C.; Dale, J. G.; Noack, C. W.; Yang, T.; Brown, G. E.; Lowry, G. V. Sulfidation of Copper Oxide Nanoparticles and Properties of Resulting Copper Sulfide. *Environmental Science-Nano* **2014**, *1*, 347-357.
14. Wang, Z.; von dem Bussche, A.; Kabadi, P. K.; Kane, A. B.; Hurt, R. H. Biological and Environmental Transformations of Copper-Based Nanomaterials. *ACS Nano* **2013**, *7*, 8715-8727.

15. Lowry, G. V.; Espinasse, B. P.; Badireddy, A. R.; Richardson, C. J.; Reinsch, B. C.; Bryant, L. D.; Bone, A. J.; Deonarine, A.; Chae, S.; Therezien, M., et al. Long-Term Transformation and Fate of Manufactured Ag Nanoparticles in a Simulated Large Scale Freshwater Emergent Wetland. *Environ. Sci. Technol.* **2012**, *46*, 7027-7036.
16. Buffet, P. E.; Tankoua, O. F.; Pan, J. F.; Berhanu, D.; Herrenknecht, C.; Poirier, L.; Amiard-Triquet, C.; Amiard, J. C.; Berard, J. B.; Risso, C., et al. Behavioural and Biochemical Responses of Two Marine Invertebrates *Scrobicularia Plana* and *Hediste Diversicolor* to Copper Oxide Nanoparticles. *Chemosphere* **2011**, *84*, 166-174.
17. Heinlaan, M.; Kahru, A.; Kasemets, K.; Arbeille, B.; Prensier, G.; Dubourguier, H. C. Changes in the *Daphnia Magna* Midgut Upon Ingestion of Copper Oxide Nanoparticles: A Transmission Electron Microscopy Study. *Water Res.* **2011**, *45*, 179-190.
18. Adeleye, A. S.; Conway, J. R.; Perez, T.; Rutten, P.; Keller, A. A. Influence of Extracellular Polymeric Substances on the Long-Term Fate, Dissolution, and Speciation of Copper-Based Nanoparticles. *Environ. Sci. Technol.* **2014**, *48*, 12561-12568.
19. Gottschalk, F.; Sonderer, T.; Scholz, R. W.; Nowack, B. Modeled Environmental Concentrations of Engineered Nanomaterials (TiO₂, ZnO, Ag, CNT, Fullerenes) for Different Regions. *Environ. Sci. Technol.* **2009**, *43*, 9216-9222.
20. Mueller, N. C.; Nowack, B. Exposure Modeling of Engineered Nanoparticles in the Environment. *Environ. Sci. Technol.* **2008**, *42*, 4447-4453.
21. Keller, A. A.; Lazareva, A. Predicted Releases of Engineered Nanomaterials: From Global to Regional to Local. *Environmental Science & Technology Letters* **2014**, *1*, 65-70.
22. Fleming, C. A.; Trevors, J. T. Copper Toxicity and Chemistry in the Environment: A Review. *Water Air and Soil Pollution* **1989**, *44*, 143-158.
23. Kramer, K. J. M.; Jak, R. G.; van Hattum, B.; Hooftman, R. N.; Zwolsman, J. J. G. Copper Toxicity in Relation to Surface Water-Dissolved Organic Matter: Biological Effects to *Daphnia Magna*. *Environ. Toxicol. Chem.* **2004**, *23*, 2971-2980.
24. Hoffmann, S. R.; Shafer, M. M.; Armstrong, D. E. Strong Colloidal and Dissolved Organic Ligands Binding Copper and Zinc in Rivers. *Environ. Sci. Technol.* **2007**, *41*, 6996-7002.
25. Wang, L. F.; Habibul, N.; He, D. Q.; Li, W. W.; Zhang, X.; Jiang, H.; Yu, H. Q. Copper Release from Copper Nanoparticles in the Presence of Natural Organic Matter. *Water Res.* **2015**, *68*, 12-23.
26. Edwards, M.; Sprague, N. Organic Matter and Copper Corrosion By-Product Release: A Mechanistic Study. *Corrosion Science* **2001**, *43*, 1-18.
27. Conway, J. R.; Adeleye, A. S.; Gardea-Torresdey, J.; Keller, A. A. Aggregation, Dissolution, and Transformation of Copper Nanoparticles in Natural Waters. *Environ. Sci. Technol.* **2015**, *49*, 2749-2756.
28. Markus, A. A.; Parsons, J. R.; Roex, E. W. M.; de Voogt, P.; Laane, R. Modeling Aggregation and Sedimentation of Nanoparticles in the Aquatic Environment. *Sci. Total Environ.* **2015**, *506*, 323-329.
29. He, D.; Bligh, M. W.; Waite, T. D. Effects of Aggregate Structure on the Dissolution Kinetics of Citrate-Stabilized Silver Nanoparticles. *Environ. Sci. Technol.* **2013**, *47*, 9148-9156.
30. Liu, J.; Aruguete, D. M.; Murayama, M.; Hochella, M. F. Influence of Size and Aggregation on the Reactivity of an Environmentally and Industrially Relevant Nanomaterial (PbS). *Environ. Sci. Technol.* **2009**, *43*, 8178-8183.

31. Rubasinghege, G.; Lentz, R. W.; Park, H.; Scherer, M. M.; Grassian, V. H. Nanorod Dissolution Quenched in the Aggregated State. *Langmuir* **2010**, *26*, 1524-1527.
32. Vikesland, P. J.; Heathcock, A. M.; Rebodos, R. L.; Makus, K. E. Particle Size and Aggregation Effects on Magnetite Reactivity toward Carbon Tetrachloride. *Environ. Sci. Technol.* **2007**, *41*, 5277-5283.
33. Hotze, E. M.; Bottero, J. Y.; Wiesner, M. R. Theoretical Framework for Nanoparticle Reactivity as a Function of Aggregation State. *Langmuir* **2010**, *26*, 11170-11175.
34. Lok, C. N.; Ho, C. M.; Chen, R.; He, Q. Y.; Yu, W. Y.; Sun, H.; Tam, P. K. H.; Chiu, J. F.; Che, C. M. Silver Nanoparticles: Partial Oxidation and Antibacterial Activities. *J. Biol. Inorg. Chem.* **2007**, *12*, 527-534.
35. Kvittek, L.; Panacek, A.; Soukupova, J.; Kolar, M.; Vecerova, R.; Pucek, R.; Holecova, M.; Zboril, R. Effect of Surfactants and Polymers on Stability and Antibacterial Activity of Silver Nanoparticles (NPs). *J. Phys. Chem. C* **2008**, *112*, 5825-5834.
36. Haynes, C. L.; Van Duyne, R. P. Nanosphere Lithography: A Versatile Nanofabrication Tool for Studies of Size-Dependent Nanoparticle Optics. *J. Phys. Chem. B* **2001**, *105*, 5599-5611.
37. Kent, R. D.; Vikesland, P. J. Controlled Evaluation of Silver Nanoparticle Dissolution Using Atomic Force Microscopy. *Environ. Sci. Technol.* **2012**, *46*, 6977-6984.
38. Kent, R. D.; Oser, J. G.; Vikesland, P. J. Controlled Evaluation of Silver Nanoparticle Sulfidation in a Full-Scale Wastewater Treatment Plant. *Environ. Sci. Technol.* **2014**, *48*, 8564-8572.
39. Chen, K.; Stoianov, S. V.; Bangerter, J.; Robinson, H. D. Restricted Meniscus Convective Self-Assembly. *J. Colloid Interface Sci.* **2010**, *344*, 315-320.
40. Liu, J. Y.; Hurt, R. H. Ion Release Kinetics and Particle Persistence in Aqueous Nano-Silver Colloids. *Environ. Sci. Technol.* **2010**, *44*, 2169-2175.
41. Liu, J. Y.; Sonshine, D. A.; Shervani, S.; Hurt, R. H. Controlled Release of Biologically Active Silver from Nanosilver Surfaces. *ACS Nano* **2010**, *4*, 6903-6913.
42. House, J. E., *Principles of Chemical Kinetics*. 2 ed.; Academic Press: Burlington, 2007.
43. Gondikas, A. P.; Morris, A.; Reinsch, B. C.; Marinakos, S. M.; Lowry, G. V.; Hsu-Kim, H. Cysteine-Induced Modifications of Zero-Valent Silver Nanomaterials: Implications for Particle Surface Chemistry, Aggregation, Dissolution, and Silver Speciation. *Environ. Sci. Technol.* **2012**, *46*, 7037-7045.
44. Zhang, X. Y.; Hicks, E. M.; Zhao, J.; Schatz, G. C.; Van Duyne, R. P. Electrochemical Tuning of Silver Nanoparticles Fabricated by Nanosphere Lithography. *Nano Lett.* **2005**, *5*, 1503-1507.
45. Hsu, M.-S.; Cao, Y.-W.; Wang, H.-W.; Pan, Y.-S.; Lee, B.-H.; Huang, C.-L. Time-Dependent Surface Plasmon Resonance Spectroscopy of Silver Nanoprisms in the Presence of Halide Ions. *Chemphyschem* **2010**, *11*, 1742-1748.
46. Downs, R. T. In *The Ruff Project: An Integrated Study of the Chemistry, Crystallography, Raman and Infrared Spectroscopy of Minerals*, Program and Abstracts of the 19th General Meeting of the International Mineralogical Association, Kobe, Japan, July 23-28, 2006; International Mineralogical Association: Kobe, Japan, 2006.
47. Biesinger, M. C.; Lau, L. W. M.; Gerson, A. R.; Smart, R. S. C. Resolving Surface Chemical States in XPS Analysis of First Row Transition Metals, Oxides and Hydroxides: Sc, Ti, V, Cu and Zn. *Applied Surface Science* **2010**, *257*, 887-898.

48. Kundu, M.; Hasegawa, T.; Terabe, K.; Yamamoto, K.; Aono, M. Structural Studies of Copper Sulfide Films: Effect of Ambient Atmosphere. *Science and Technology of Advanced Materials* **2008**, *9*.
49. Levard, C.; Reinsch, B. C.; Michel, F. M.; Oumahi, C.; Lowry, G. V.; Brown, G. E. Sulfidation Processes of PVP-Coated Silver Nanoparticles in Aqueous Solution: Impact on Dissolution Rate. *Environ. Sci. Technol.* **2011**, *45*, 5260-5266.
50. Ma, R.; Levard, C.; Michel, F. M.; Brown, G. E.; Lowry, G. V. Sulfidation Mechanism for Zinc Oxide Nanoparticles and the Effect of Sulfidation on Their Solubility. *Environ. Sci. Technol.* **2013**, *47*, 2527-2534.
51. Donner, E.; Howard, D. L.; de Jonge, M. D.; Paterson, D.; Cheah, M. H.; Naidu, R.; Lombi, E. X-Ray Absorption and Micro X-Ray Fluorescence Spectroscopy Investigation of Copper and Zinc Speciation in Biosolids. *Environ. Sci. Technol.* **2011**, *45*, 7249-7257.
52. Lombi, E.; Donner, E.; Taheri, S.; Tavakkoli, E.; Jamting, A. K.; McClure, S.; Naidu, R.; Miller, B. W.; Scheckel, K. G.; Vasilev, K. Transformation of Four Silver/Silver Chloride Nanoparticles During Anaerobic Treatment of Wastewater and Post-Processing of Sewage Sludge. *Environ. Pollut.* **2013**, *176*, 193-197.
53. Reinsch, B. C.; Levard, C.; Li, Z.; Ma, R.; Wise, A.; Gregory, K. B.; Brown, G. E.; Lowry, G. V. Sulfidation of Silver Nanoparticles Decreases *Escherichia Coli* Growth Inhibition. *Environ. Sci. Technol.* **2012**, *46*, 6992-7000.
54. Rozan, T. F.; Lassman, M. E.; Ridge, D. P.; Luther, G. W. Evidence for Iron, Copper and Zinc Complexation as Multinuclear Sulphide Clusters in Oxic Rivers. *Nature* **2000**, *406*, 879-882.
55. DePalma, S. G. S.; Arnold, W. R.; McGeer, J. C.; Dixon, D. G.; Smith, D. S. Effects of Dissolved Organic Matter and Reduced Sulphur on Copper Bioavailability in Coastal Marine Environments. *Ecotox. Environ. Safe.* **2011**, *74*, 230-237.
56. Morones, J. R.; Elechiguerra, J. L.; Camacho, A.; Holt, K.; Kouri, J. B.; Ramirez, J. T.; Yacaman, M. J. The Bactericidal Effect of Silver Nanoparticles. *Nanotechnology* **2005**, *16*, 2346-2353.
57. Heinlaan, M.; Ivask, A.; Blinova, I.; Dubourguier, H. C.; Kahru, A. Toxicity of Nanosized and Bulk ZnO, CuO and TiO₂ to Bacteria *Vibrio Fischeri* and Crustaceans *Daphnia Magna* and *Thamnocephalus Platyurus*. *Chemosphere* **2008**, *71*, 1308-1316.
58. Edwards, M.; Schock, M. R.; Meyer, T. E. Alkalinity, pH, and Copper Corrosion by-Product Release. *Journal American Water Works Association* **1996**, *88*, 81-94.

FIGURES

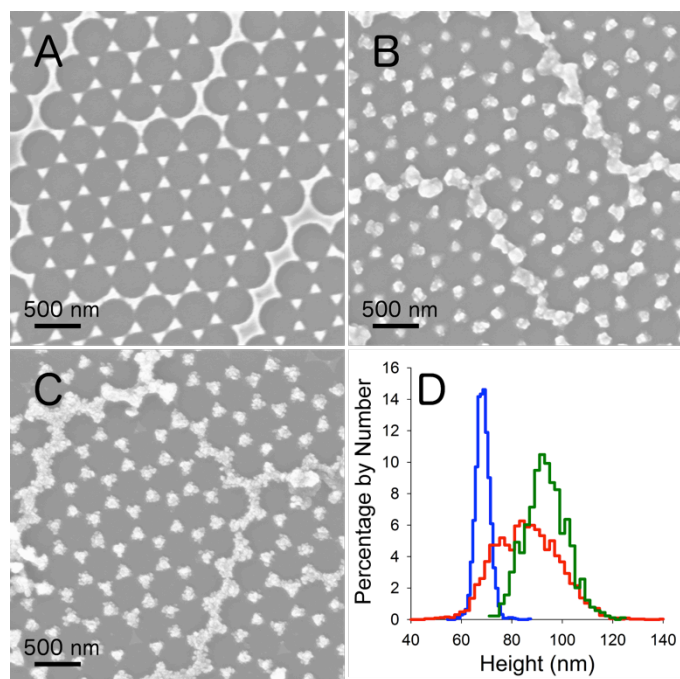


Figure 3-1. SEM micrographs of A) Cu, B) CuO/Cu(OH)₂, and C) Cu_xS NPs. D) Height distributions of Cu (blue), CuO/Cu(OH)₂ (red), and Cu_xS (green) NPs measured by AFM.

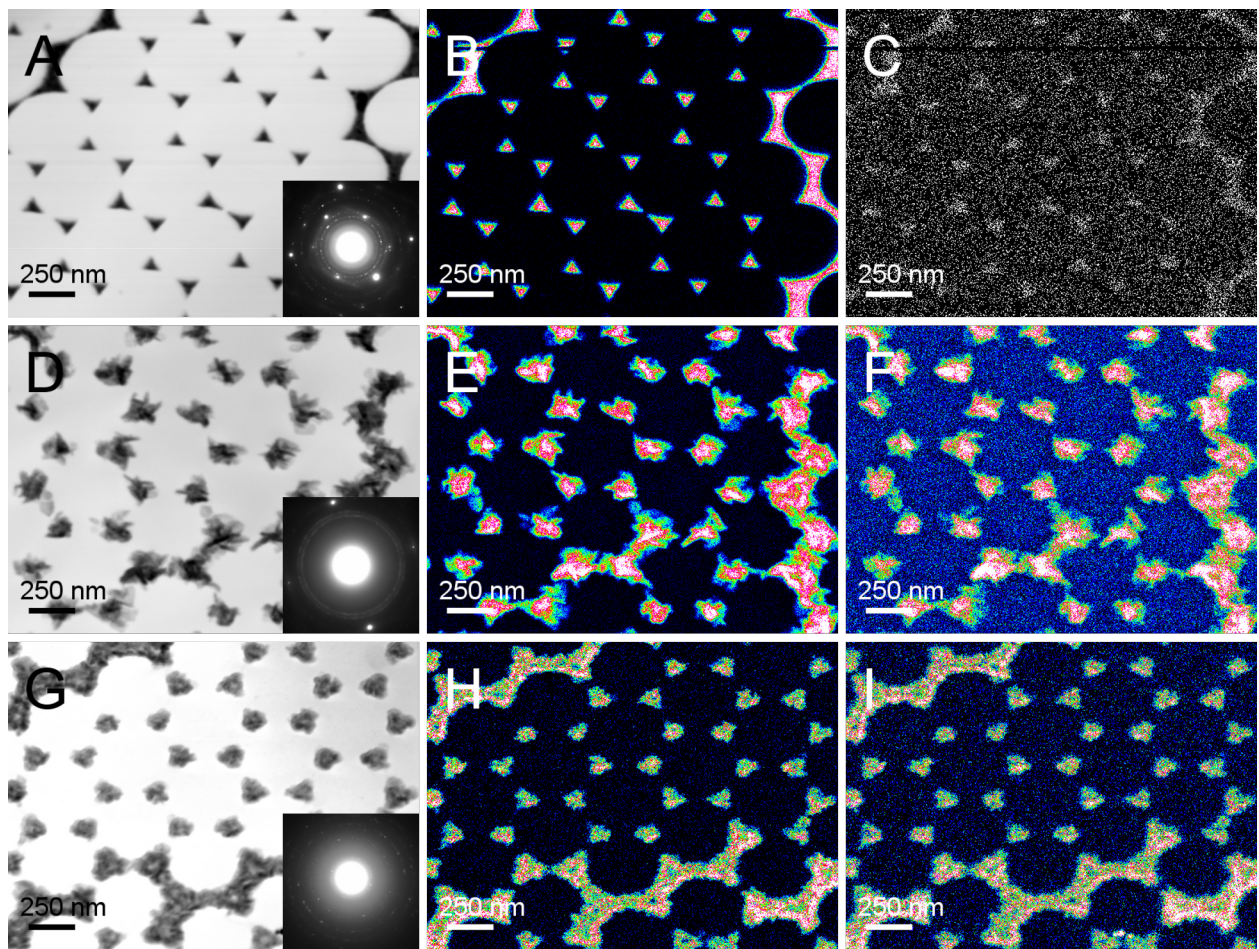


Figure 3-2. Bright field STEM images of A) Cu NPs, D) CuO/Cu(OH)₂ NPs, and G) Cu_xS NPs. Inset: SAED pattern from the respective sample. EDS maps of B) Cu and C) O for Cu NPs, E) Cu and F) O for CuO/Cu(OH)₂ NPs, and H) Cu and I) S for Cu_xS NPs.

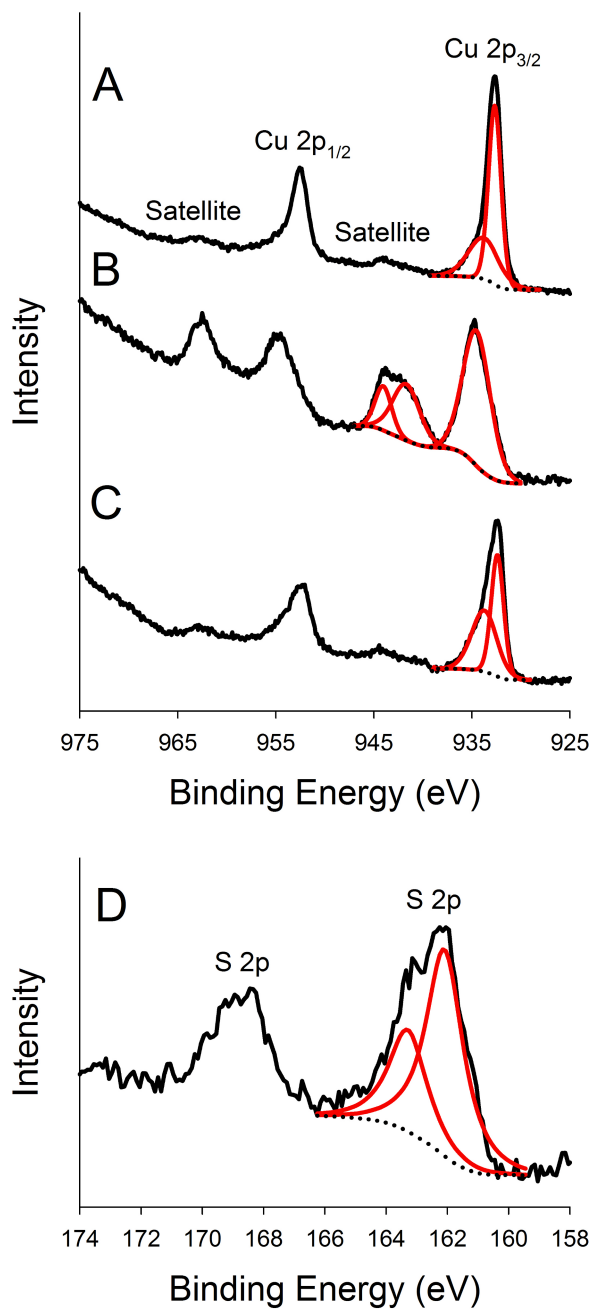


Figure 3-3. XPS spectra of A) Cu, B) CuO/Cu(OH)₂, and C) Cu_xS NPs in the Cu 2p region. D) XPS spectra of Cu_xS NPs in the S 2p region.

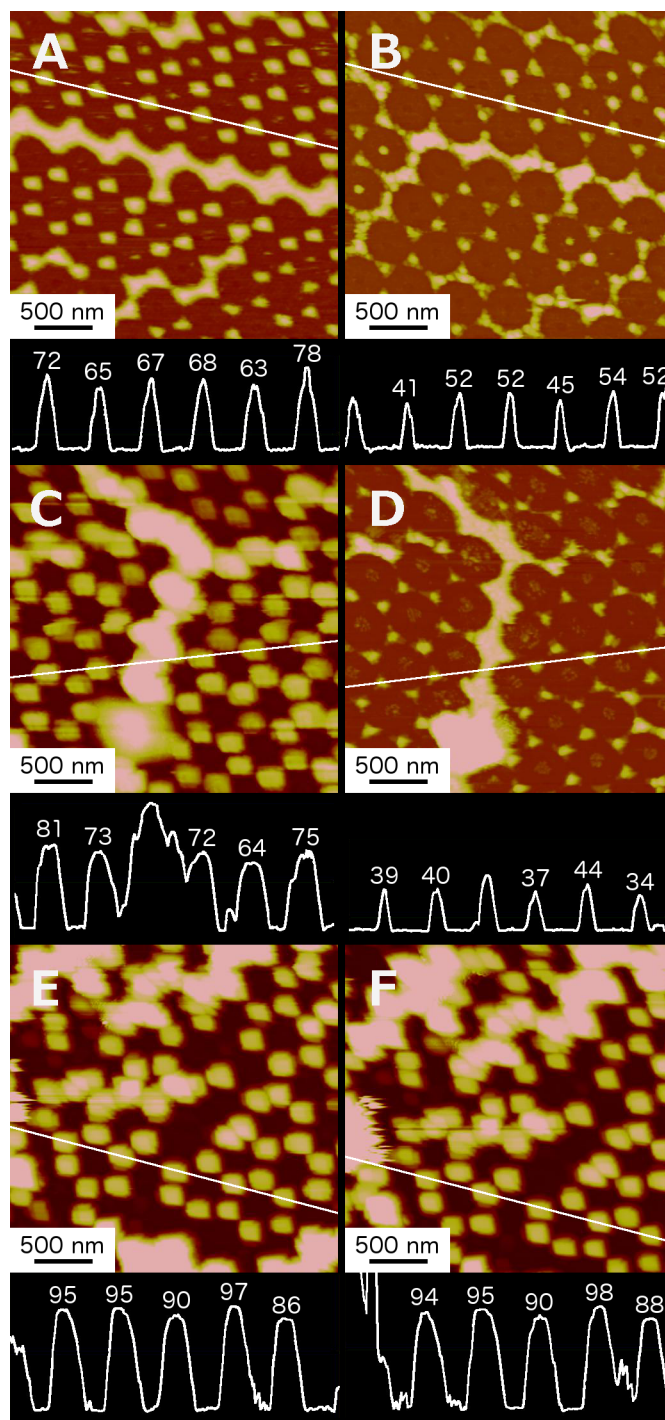


Figure 3-4. Representative AFM height images and cross-sections of Cu NPs A) before and B) after 6 h, CuO/Cu(OH)₂ NPs C) before and D) after 1 h, and Cu_xS NPs E) before and F) after 6 h in DI water (pH 5.6) with a 2 mL/min flow rate. Heights in cross sections are all in units of nm.

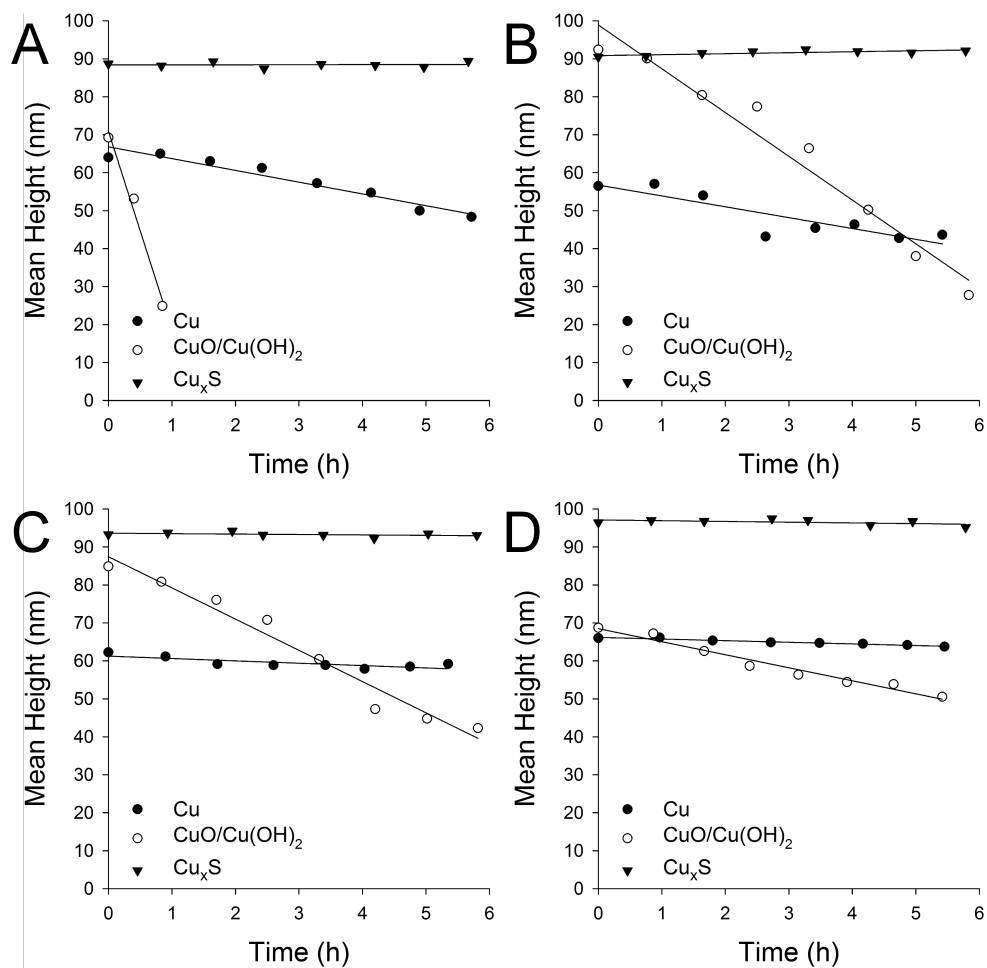


Figure 3-5. Representative time series of Cu-based NP mean heights measured by AFM under a 2 mL/min flow rate at pH A) 5.6, B) 6.6, C) 8.4, and D) 11.3.

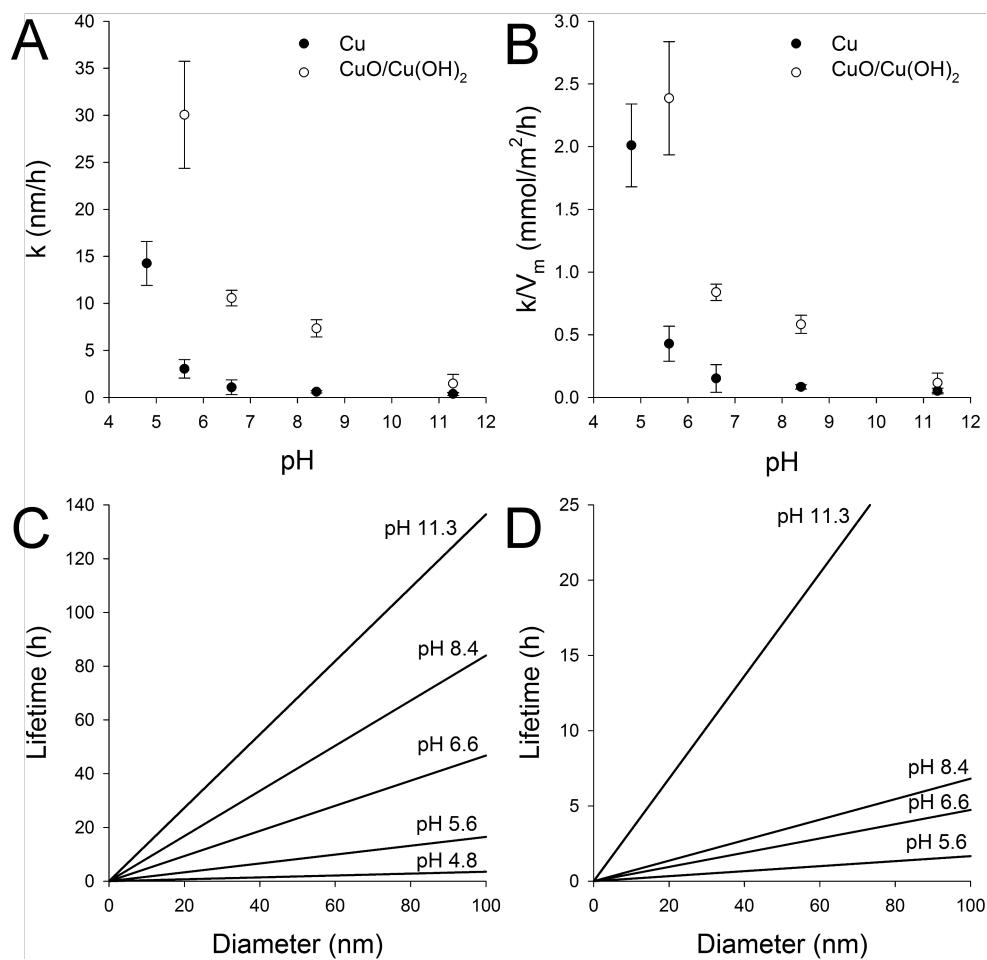


Figure 3-6. A) Dissolution rate constants and B) surface area normalized dissolution rates for Cu and CuO/Cu(OH)₂ NPs at various pH. Error bars represent standard errors from at least triplicate experimental runs. Particle lifetime as a function of initial diameter for C) Cu and D) CuO/Cu(OH)₂ NPs (note the different vertical scales).

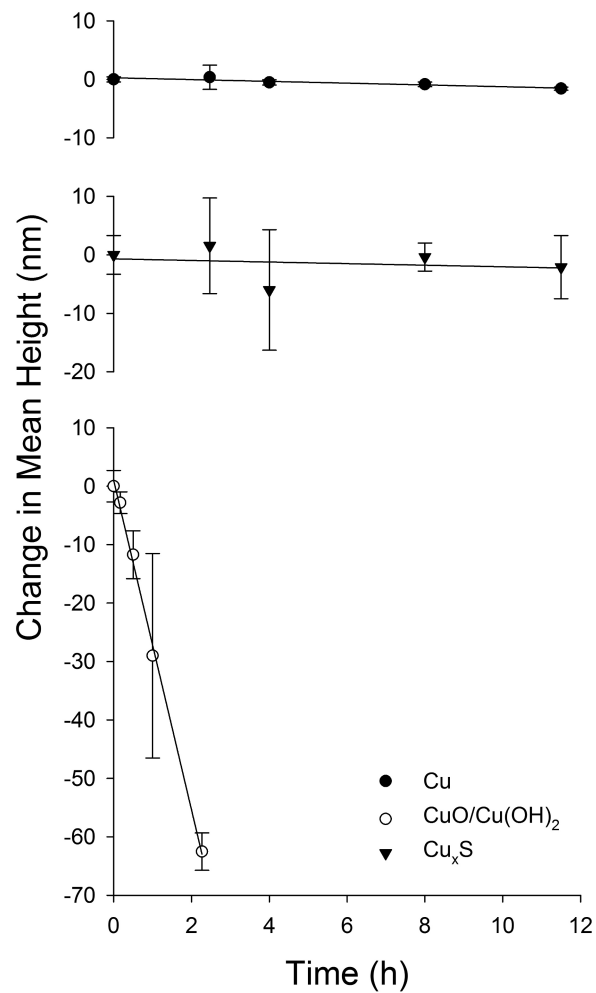


Figure 3-7. Change in mean height of Cu, CuO/Cu(OH)₂, and Cu_xS NPs over time in Stroubles Creek. Error bars represent standard deviations of triplicate specimens.

4 Conclusions

This work overcame the limitations of previous research by utilizing nanosphere lithography (NSL) to produce metal-based nanoparticle (MNP) samples that could be deployed in the field for environmentally realistic investigations of MNP transformations. Sulfidation of Ag NPs and dissolution of Cu-based NPs were both investigated for this dissertation project. Ag NP specimens were deployed in a full-scale wastewater treatment plant (WWTP). It was discovered that Ag NPs became completely sulfidized within about 1 week in anaerobic regions of the plant. Ag NPs tend to associate with the mixed liquor suspended solids of wastewater, and solid retention times in many activated sludge treatment plants are commonly greater than 1 week; thus, the results lead to the prediction that Ag NPs will primarily be in the form of Ag_2S when they exit WWTPs. Because Ag_2S is less toxic than Ag, WWTPs and sewer systems will act as sentinels to detoxify many Ag NPs before they enter natural aquatic systems.

Although a controlled experiment of Ag NP sulfidation in a full-scale WWTP had not been performed before, the conclusions derived from this field deployment were similar to the conclusions of previous bench and pilot-scale studies on the same subject. In contrast, the results of the dissolution experiments with Cu-based NPs yielded original insights into the environmental persistence of these nanomaterials. Specifically, it was found that $\text{CuO}/\text{Cu}(\text{OH})_2$ NPs would not be persistent in the environment, even at circumneutral pH. Previous studies had observed limited dissolution of CuO NPs at neutral to basic pH, consistent with the low solubility of cupric oxides; however, the dilute environmental concentrations of copper species and the abundance of natural ligands ensures that Cu-based NPs will frequently find themselves in unsaturated solutions in the environment. We demonstrated that $\text{CuO}/\text{Cu}(\text{OH})_2$ NPs dissolve rapidly in these unsaturated conditions. Based on the results of this study, Cu NPs are also

expected to be relatively short-lived in uncontaminated freshwaters, with lifetimes of several hours to several weeks. Cu_xS NPs are much more persistent than either Cu or CuO/Cu(OH)_2 NPs, but they are also expected to be less toxic. Overall, the results from the research performed for this dissertation lead toward the conclusion that environmental transformations will prevent MNPs from exerting novel toxic effects in aquatic environments.

Appendix A: Supplemental Information for Chapter 2

Crystallinity of Unsulfidized Ag NPs Produced by NSL. Unsulfidized Ag NPs produced by NSL were studied by TEM to determine their crystallinity. A high resolution TEM image of one such Ag NP and the corresponding FFT are shown in Figure A-1. The d-spacings measured for this particle were 2.36, 2.10, 1.43, 1.22, and 1.18 Å. These measurements closely match the reported d-spacings of the [111], [200], [220], [311], and [222] planes of FCC silver, which are 2.36, 2.04, 1.44, 1.23, and 1.18 Å, respectively.¹ Bright field and dark field TEM images of another unsulfidized Ag NP are shown in Figure A-2. Each dark field image highlights a different crystal face of the particle. It is evident from the dark field images that the particle does not consist of a single crystal. Based on our TEM analysis, we conclude that pristine Ag NPs produced by NSL are polycrystalline FCC silver.

In addition to the primary Ag NPs produced by the NSL procedure, numerous secondary Ag NPs were generated (Figure A-3). The smaller Ag NPs (2-10 nm) are shown surrounding the larger Ag NPs in Figure A-3A. One of the secondary Ag NPs and its FFT are shown in Figures A-3B and A-3C, respectively. The FFT reveals that the secondary Ag NPs are also polycrystalline FCC silver (d-spacings of 1.18, 1.23, 1.45, 2.04, and 2.36 Å correspond to the [222], [311], [220], [200], and [111] planes of FCC silver, respectively).¹ These secondary Ag NPs remain on the TEM grids after sulfidation and can be seen in Figures 2-2A and 2-6A.

HRTEM of Particle I. High resolution TEM images and corresponding FFTs of Particle I (Figure 2-2A) are shown in Figure A-4. The spacing of the lattice fringes shown in Figure A-4A is 2.36 Å, which corresponds to the [111] crystal plane of FCC silver.¹ Although the EDS results show that the particle's conversion to silver sulfide was almost entirely complete, it appears that a small portion at the edge remained silver metal as was the case for Particle II

(Figure 2-3); however, acanthite's $[-103]$ plane has a d-spacing of 2.38 \AA ,¹ and not enough spots appear in the FFT to conclusively determine that the lattice fringes shown in Figure A-4A belong to FCC silver and not acanthite. Figure A-4C illustrates that large portions of Particle I did not display any lattice fringes, which is characteristic of amorphous material. Lattice fringes spaced at 3.44 \AA in the lower right corner correspond to the $[-111]$ crystal plane of acanthite, but Particle I had a general lack of lattice fringes elsewhere. The FFT shows several faint spots that could not be used to identify any particular crystal structure; however, the presence of these spots may signify that crystalline material underlies an amorphous material. The presence of amorphous Ag_2S is not surprising because Levard et al. found in their study that nearly two-thirds of the Ag_2S formed by sulfidation of Ag NPs was amorphous.²

Batch Sludge Exposure. Sludge samples were collected from the Christiansburg, VA municipal wastewater treatment plant and consisted of 25% primary sludge and 75% secondary sludge. These samples were stored in 50-mL polypropylene tubes (Corning) at $4 \text{ }^\circ\text{C}$ for up to two months. It is unclear how microbial activity or other parameters such as pH may have changed during the storage period. Prepared specimens were placed in 50-mL polypropylene tubes and immersed in 10 mL of sludge for 6 d. Specimens were removed intermittently for AFM measurements. TEM grids were placed in 50-mL glass beakers and immersed in 20 mL of sludge for 2 d. Upon completion of the 6 d exposure to sludge, specimens were exposed to 10 mL of 500 mM NaCl solution and removed periodically to conduct AFM measurements. These experiments did not simulate any particular environmental process. Rather, they demonstrated the utility of our method for studies of environmental transformations in complex media. The retention of the original NSL pattern following a 6-d exposure to sewage sludge is illustrated in Figure A-5.

The mean Ag NP height increased by an average factor of 1.18 within 2 d of exposure and remained constant thereafter (Figure A-6A). Following the 6-d sludge exposure, the two specimens were introduced into a 500 mM NaCl solution. No significant change in the mean height was observed over a 2-wk dissolution period (Figure A-6B). One interpretation of these results is that the Ag NPs became sulfidized within 2 d of exposure to sludge and thus became resistant to dissolution. Although the factor of 1.18 is closer to the theoretical value of conversion from silver metal to acanthite, a comparison with the experiments in Na₂S solutions suggests that only partial sulfidation occurred in sludge. Sulfide concentration, DO, and pH were not monitored during the exposure, so we can only speculate why sulfidation was not complete. It is possible that the sludge became aerobic during the exposure period. The samples were sealed during exposure, but the seals were not airtight. Molecular oxygen can inhibit the production of H₂S by sulfate-reducing bacteria in wastewater, and it can also trigger the oxidation of H₂S mediated by sulfide-oxidizing bacteria; thus, infiltration of oxygen into the sludge mixture could have depleted the sulfide concentration until sulfidation ceased. Alternatively, microbial production of organic acids could have caused a decrease in pH that led to rapid volatilization of hydrogen sulfide gas. It is also possible that insufficient sulfide was present in the sludge initially to result in complete sulfidation of Ag NPs. Results from field deployment of Ag NPs in a full-scale WWTP showed that sulfidation continued until completion under more environmentally relevant conditions; thus, the partial sulfidation of Ag NPs in our sludge experiments is probably due to an unrealistic exposure scenario instead of an effect that would be expected in the environment.

TEM and EDS were performed following a 2-d exposure to sludge (Figure A-7). Sulfur signals were detected on all 5 particles shown in Figure A-7A, with an average Ag:S atomic ratio

of 6.9 and a minimum of 3.0. Because the ratio was always greater than 2, these results suggest that the sulfidation reaction was not complete during the 2-d exposure, in agreement with the AFM results. EDS spectra taken at different locations on the same particle varied greatly in their sulfur content, with an Ag:S ratio of 3.0 at one location (S = 0.4 at.%) and 107 at another (S = 0.01 at.%), which illustrates the non-uniform nature of sulfidation in sludge. An intense C peak appeared in all the EDS spectra of Ag NPs exposed to sewage sludge. Also, a ~2-nm thick layer of amorphous material is apparent near the edge of the Ag NP in Figure A-7C. Thus, it appears that organic material adsorbed to the Ag NPs during the sludge exposure. An FFT analysis of the high resolution TEM image shown in Figure A-7C revealed d-spacings of 5.16, 2.57, 1.70, and 1.27 Å. The most prominent spots in a computer simulated diffraction pattern of acanthite gave a close match of the pattern observed in the FFT—the predicted d-spacings were 5.17, 2.58, 1.72, and 1.29 Å.

SEM/EDS of Ag NPs from Field Study. Figure A-8 shows a typical SEM image and EDS spectra for Ag NPs that had been deployed in the anoxic zone of the WWTP's activated sludge basin for 7 d. The Ag and S signals are both very low compared to the background signal, but they are clearly detectable and indicate a high degree of sulfidation for this specimen.

REFERENCES

1. Downs, R. T. In *The RRUFF project: An integrated study of the chemistry, crystallography, Raman and infrared spectroscopy of minerals*, Program and Abstracts of the 19th General Meeting of the International Mineralogical Association, Kobe, Japan, July 23-28, 2006; International Mineralogical Association: Kobe, Japan, 2006.
2. Levard, C.; Reinsch, B. C.; Michel, F. M.; Oumahi, C.; Lowry, G. V.; Brown, G. E. Sulfidation processes of PVP-coated silver nanoparticles in aqueous solution: Impact on dissolution rate. *Environ. Sci. Technol.* **2011**, *45*, 5260-5266.

FIGURES

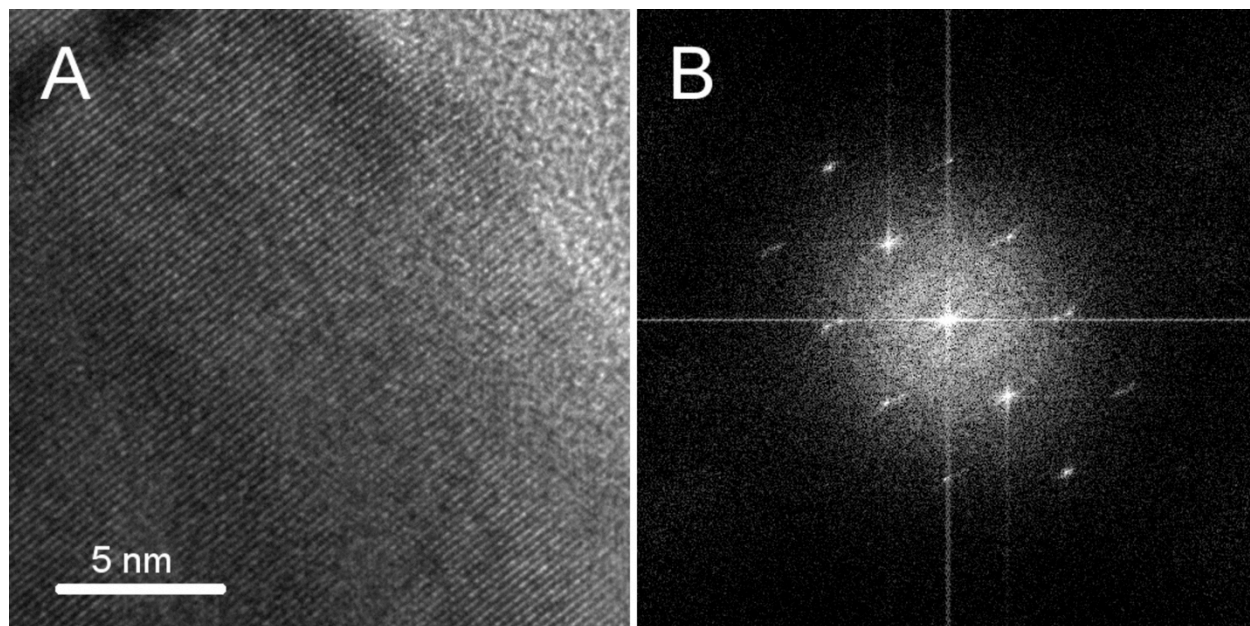


Figure A-1. A) High resolution TEM image of an unsulfidized Ag NP produced by NSL. B) FFT of A.

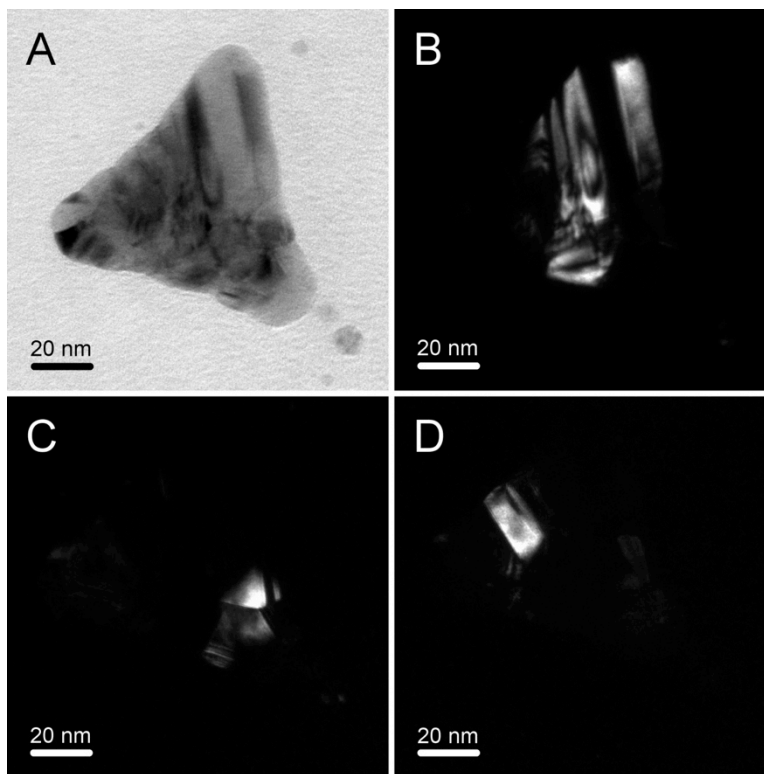


Figure A-2. A) Bright field TEM image of an unsulfidized Ag NP produced by NSL. B-D) Dark field TEM images of the particle shown in A.

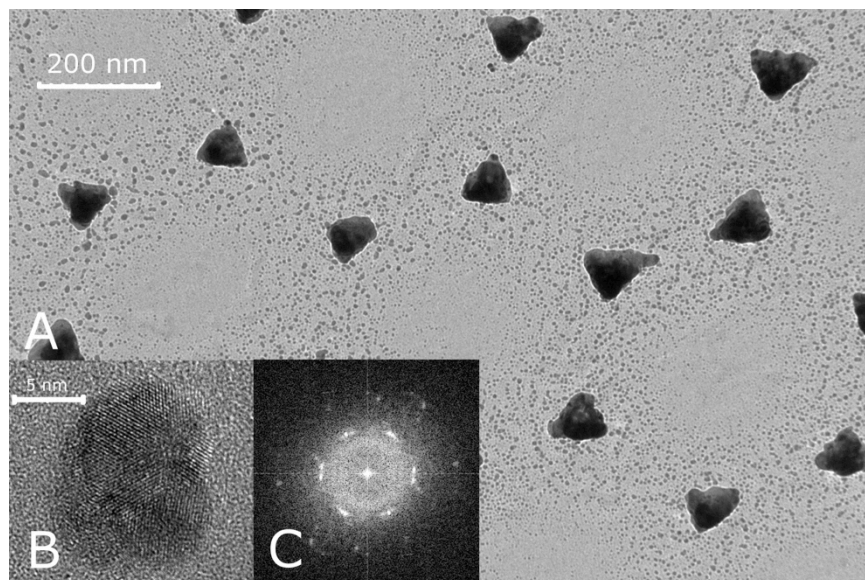


Figure A-3. A) Bright field TEM image of an unsulfidized Ag NP array produced by NSL. B) High resolution TEM image of one of the small (2-10 nm) Ag NPs produced by NSL. C) FFT of the particle shown in B.

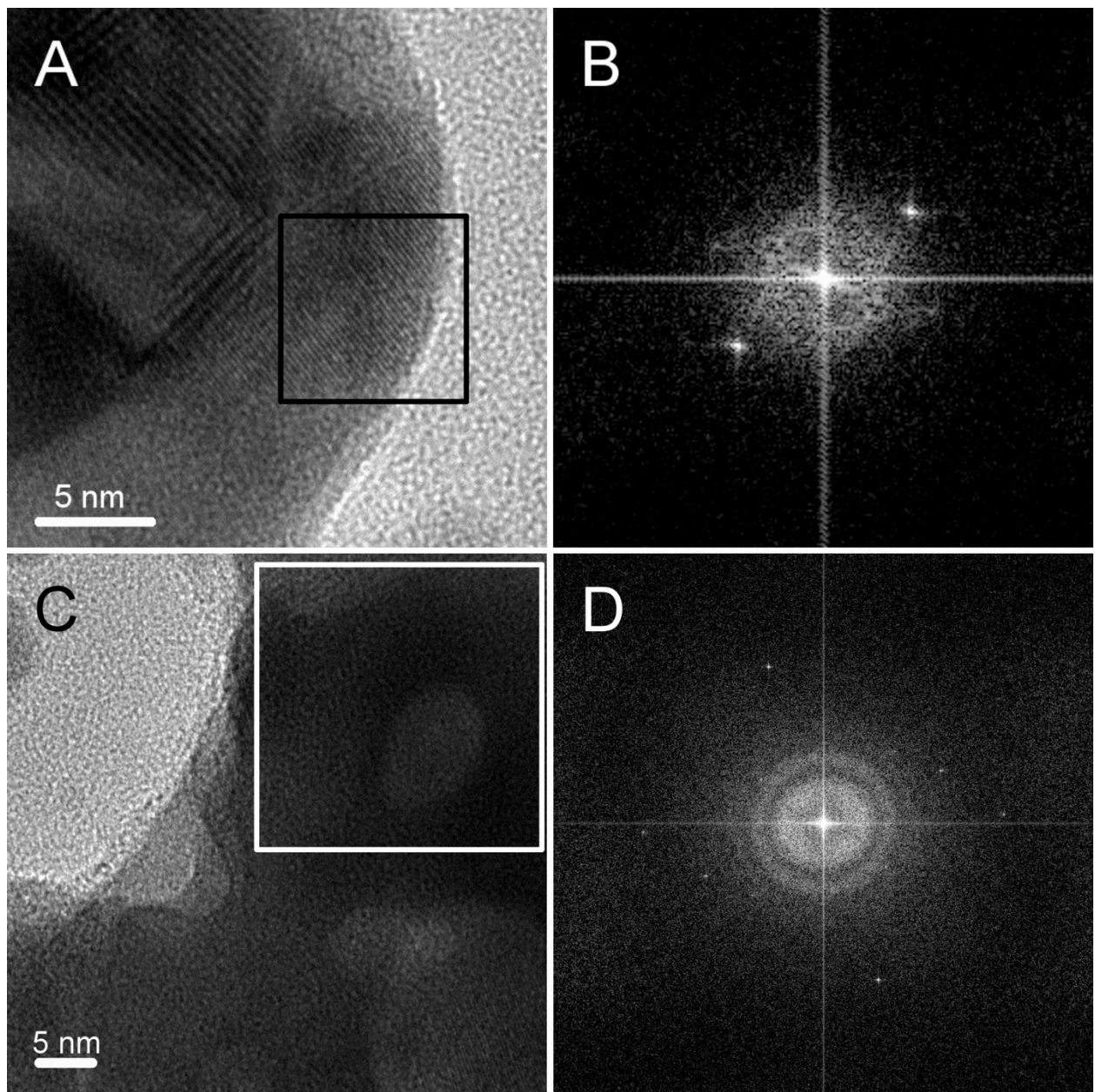


Figure A-4. A and C) High resolution TEM images of Particle I (Figure 2-2A). B and D) FFTs of the regions marked in A and C, respectively.

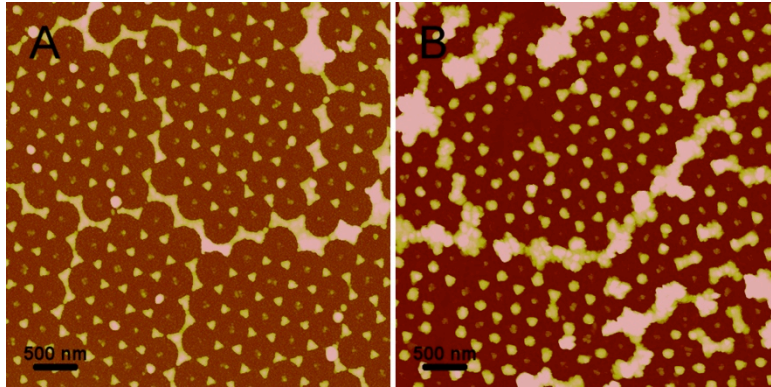


Figure A-5. Ag NPs produced by NSL A) before and B) after a 6-d exposure to sewage sludge.

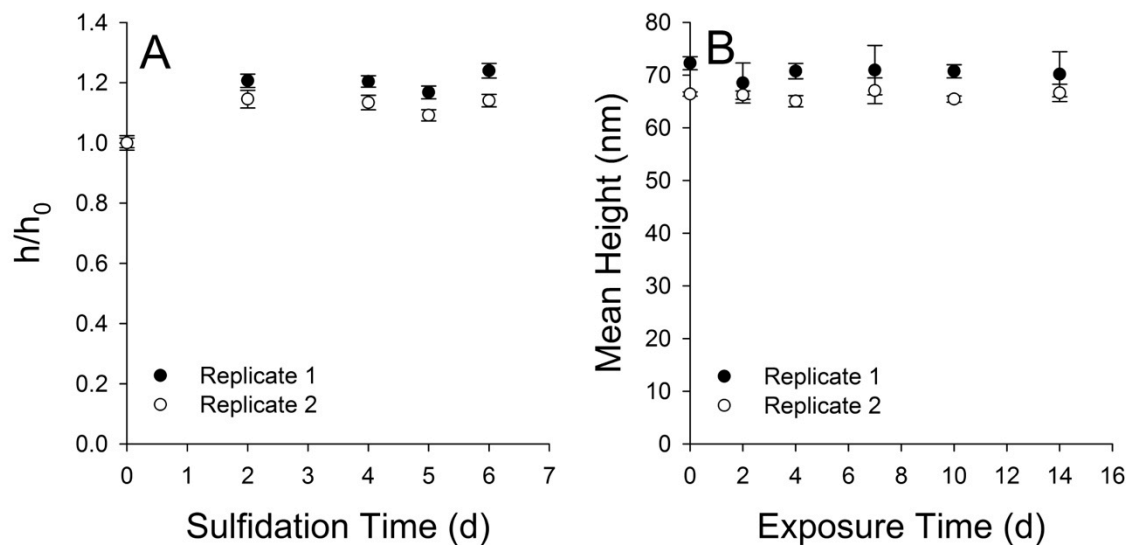


Figure A-6. A) Ratio of mean height (h) to initial mean height (h_0) measured over time by AFM for Ag NP arrays exposed to sludge from a municipal wastewater treatment plant. B) Mean height measured over time for Ag NPs exposed to 500 mM NaCl following a 6-d exposure to sludge. Error bars represent standard deviations of triplicate measurements.

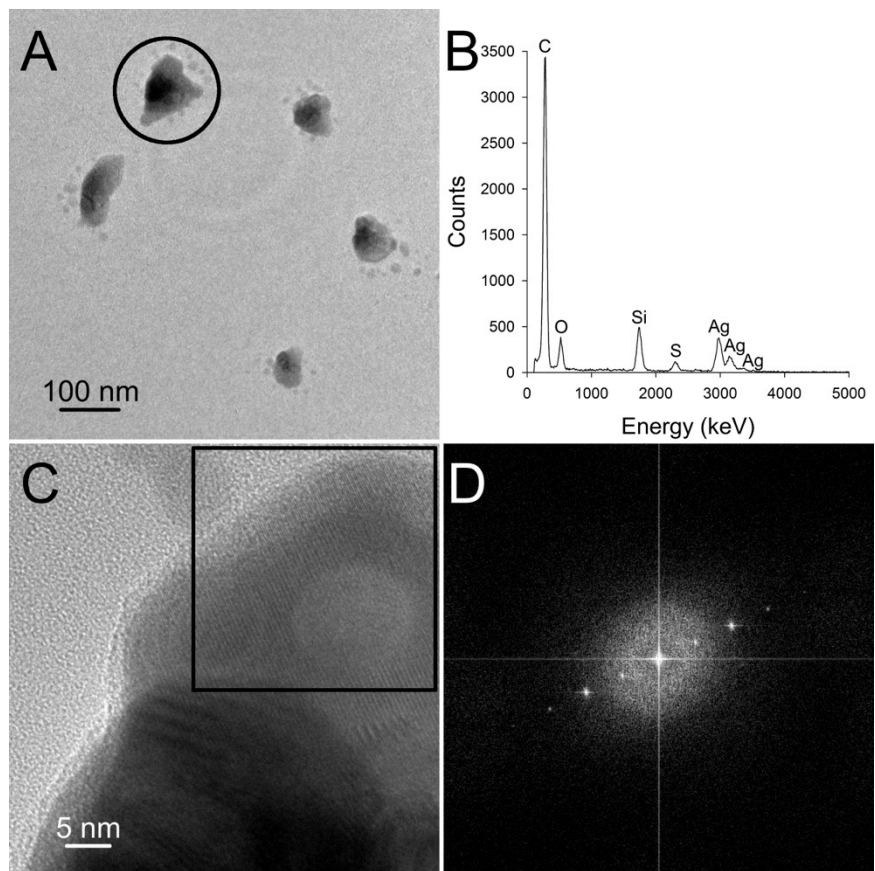


Figure A-7. A) Bright field TEM image of NSL-produced Ag NPs after a 2-d exposure to sludge from a municipal wastewater treatment plant. B) EDS spectrum and C) high resolution TEM image of the particle circled in A. D) FFT of the region marked in C.

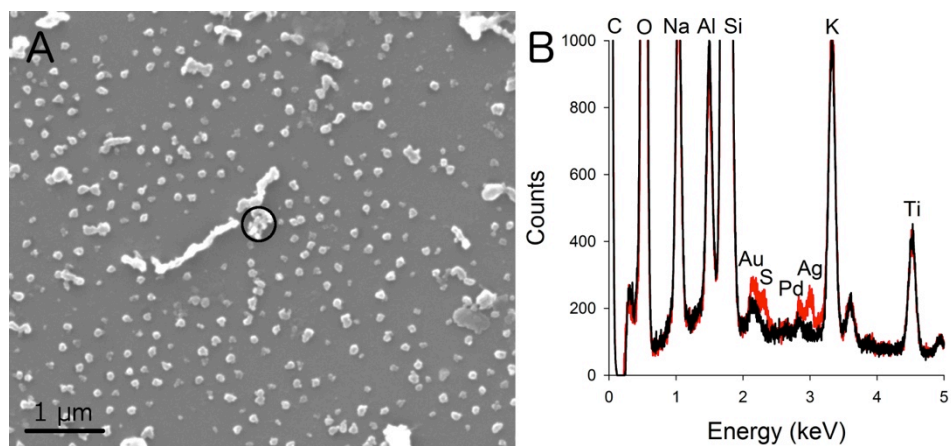


Figure A-8. A) SEM image of Ag NPs that had been deployed in the anoxic zone of the activated sludge basin of the WWTP for 7 d. B) Background EDS spectrum (black) and EDS spectrum of the small aggregate circled in A (red).

Appendix B: Supplemental Information for Chapter 3

Shift in dissolution rate. It is notable that most of the CuO/Cu(OH)_2 NP specimens dissolved at a constant rate in agreement with Equation 3-9. This result indicates that the Cu NPs had been oxidized completely. If oxidation had only been partial, then we would expect to observe two distinct slopes in the mean height time series data. In fact, we did observe such a phenomenon in a couple experimental runs with CuO/Cu(OH)_2 NPs (Figure B-1). These particular specimens exhibited rapid dissolution initially followed by an obvious decrease in the dissolution rate. This observation can be explained by partial oxidation of these specimens. A copper oxide shell formed around a metallic Cu core, and the shell dissolved rapidly. After dissolution of the shell, the slower dissolving core remained. This scenario was not observed for the majority of the CuO/Cu(OH)_2 NPs; therefore, oxidation was complete in most cases.

XPS of the C 1s region. XPS spectra for the C 1s binding region are shown in Figure B-2. The prominent peak at 284.6 eV is due to adventitious carbon. The weaker peak at 288.4 eV indicates the presence of carbonate species. The carbonate peak is present in all three samples, although it is quite weak in the Cu_xS NP specimen.

Contracting volume rate law for cylindrical nanoparticles. As discussed in the main text, nanoparticles produced by NSL initially have a truncated tetrahedral shape. The initial shape is transformed into a disk-like or cylindrical shape. This morphological change is caused by accelerated dissolution at the triangular corners where the surface energy is high.¹⁻³ A contracting volume rate law can be derived for a cylinder. We assume a cylindrical volume of height h and radius r . In our case, the particles are attached to a surface, so the height can only decrease from the top down and not from the bottom up (*i.e.*, the surface area on the bottom of

the cylinders is unavailable for reaction). The volume, V , and available surface area, A , of the cylinder are given by Equations B-1 and B-2, respectively.

$$V = \pi r^2 h \quad (\text{B-1})$$

$$A = 2\pi r h + \pi r^2 \quad (\text{B-2})$$

Differentiating Equation B-1 by the chain rule yields Equation B-3.

$$\frac{dV}{dt} = 2\pi r h \frac{dr}{dt} + \pi r^2 \frac{dh}{dt} \quad (\text{B-3})$$

If we assume $dh/dt = dr/dt$, then Equation B-3 can be factored to yield Equation B-4:

$$\frac{dV}{dt} = (2\pi r h + \pi r^2) \frac{dr}{dt} \quad (\text{B-4})$$

Substituting Equation B-2 into Equation B-4 gives Equation B-5:

$$\frac{dV}{dt} = A \frac{dr}{dt} \quad (\text{B-5})$$

Finally, by substituting Equation B-5 into the contracting volume rate law given in Equation 3-7 and then dividing both sides by A , the result simplifies to Equation 3-9. Hence, the mathematical result for a cylinder is the equivalent to the result for a sphere. Based on our previous work, the assumption of equality between the rates of change of height and radius is reasonable. The rate constants determined for NSL-produced Ag NPs dissolving in NaCl solutions were statistically the same for height and radius measurements, although the rate constants based on radius measurements were consistently lower than those based on height measurements.¹ The statistical error between the two estimates was small enough to be of little practical significance, and it may have been due to a bias in the AFM measurements. AFM probes tend to become dull after repeated scans, and the effect of this dulling is to make the lateral dimensions of objects appear larger. This source of error was not corrected for, so the time

series of radius measurements would systematically underestimate the actual decrease in the particles' lateral dimensions.

We now consider the effect of cylindrical geometry on Equation 3-11. First, assume that $h = r$, which is a close approximation for the NPs in this study.¹ Then Equation B-1 can be simplified to a cubic function of r that is the same as the equation for the volume of a sphere without the leading factor of $4/3$. Equation 3-11 is derived from Equation B-6:

$$\frac{[Cu^{z+}]}{[Cu^{z+}]_0} = 1 - \frac{[Cu^{z+}]_p}{[Cu^{z+}]_0} \quad (\text{B-6})$$

where $[Cu^{z+}]$ is the total dissolved Cu ion concentration, $[Cu^{z+}]_0$ is the initial Cu mass in the system expressed as an equivalent concentration, and $[Cu^{z+}]_p$ is the remaining Cu mass in the NPs expressed as an equivalent concentration. Both the numerator and the denominator of the second term on the right-hand side of the equation can be written in terms of the volume of a single particle. All the leading constants will cancel out by division; therefore, the result will be the same whether the volume of a sphere, a hemisphere, or a cylinder with $h = r$ is substituted into the equation.

Solution to continuous flow kinetic model. Equation 3-12 in the manuscript gives the mass balance on metal ions with the AFM liquid cell as the control volume, and it is reproduced here as Equation B-7:

$$\frac{d[Cu^{z+}]}{dt} = \frac{3[Cu^{z+}]_0}{\tau_L} \left(1 - \frac{t}{\tau_L}\right)^2 - \frac{[Cu^{z+}]}{\tau_R} \quad (\text{B-7})$$

where t is time, τ_R is the residence time, and τ_L is the particle lifetime. The initial condition is $[Cu^{z+}] = 0$. Equation B-7 is a first-order, linear, ordinary differential equation, and it can be solved analytically by the use of an integrating factor. The solution for $0 \leq t \leq \tau_L$ is

$$[Cu^{z+}] = \frac{3[Cu^{z+}]_0\tau_R}{\tau_L} \left(\left(1 - \frac{t}{\tau_L}\right)^2 + \frac{2\tau_R}{\tau_L} \left(1 - \frac{t}{\tau_L}\right) + 2 \left(\frac{\tau_R}{\tau_L}\right)^2 - \left(1 + \frac{2\tau_R}{\tau_L} + 2 \left(\frac{\tau_R}{\tau_L}\right)^2\right) e^{-t/\tau_R} \right) \quad (B-8)$$

The solution for $t > \tau_L$ is

$$[Cu^{z+}] = \frac{3[Cu^{z+}]_0\tau_R}{\tau_L} \left(2 \left(\frac{\tau_R}{\tau_L}\right)^2 - \left(1 + \frac{2\tau_R}{\tau_L} + 2 \left(\frac{\tau_R}{\tau_L}\right)^2\right) e^{-\tau_L/\tau_R} \right) e^{-(t-\tau_L)/\tau_R} \quad (B-9)$$

Concentrations calculated by Equations B-8 and B-9 for Cu and CuO/Cu(OH)₂ NPs at the various pH values tested in this research are shown in Figure B-4.

Comparison of calculated maximum total dissolved Cu concentrations and tenorite solubility. The estimated maximum total dissolved Cu concentrations, which always occur within the first few seconds of the experiment because of the low residence time, are compared with tenorite solubility in Table B-1. The calculation of tenorite solubility was performed with Visual MINTEQ (ver. 3.0) with the pH fixed at the value of interest and the temperature set to 25 °C. As noted in the main text, equilibrium with atmospheric CO₂ was not included in the thermodynamic calculations shown in Table B-1. When a fixed partial pressure of 0.00038 atm CO₂ is used in the calculation, the estimated solubility of tenorite at pH 8.4 increases to 5185 ng/L due to the formation of soluble cupric carbonate complexes. According to Visual MINTEQ calculations, tenorite is the least soluble of any cupric oxide, hydroxide, or carbonate solid phase.

Lower bound for total dissolved Cu. The model described above assumes that all the Cu mass on a substrate consists of uniformly sized NPs. As discussed in the main text, these NPs actually account for less than 26% of the total Cu mass on the substrate. Because the other nanostructures on the substrate dissolve more slowly than the NPs, the model overestimates the amount of dissolution and represents an upper bound. A lower bound can be estimated by assuming that the Cu mass consists entirely of a single thin film with thickness equivalent to the

height of the NPs. Thin films have the lowest surface area to mass ratio, and, therefore, will dissolve more slowly than any of the other Cu structures on the substrate. We assume that the thin film dissolves according to a contracting volume rate law (Equation 3-7) and that the rate constant is the same as that measured for Cu-based NPs. The area for a thin film is essentially constant until the dissolution process is nearly complete and $\tau_R \ll \tau_L$ in our system, so we assume that a steady state is achieved rapidly. The steady-state concentration is given by Equation B-10:

$$[Cu^{z+}] = \frac{[Cu^{z+}]_0 \tau_R}{\tau_L} \quad (\text{B-10})$$

where all variables are as defined above. If we consider Equation B-8, it will be noted that the leading multiplication factor is three times Equation B-10. This leading factor is also approximately equal to the maximum total dissolved Cu ion concentration because the terms in parentheses are nearly equal to 1 when t is small and $\tau_R \ll \tau_L$. Thus, our lower bound estimate of the total dissolved Cu concentration is one third of our upper estimate.

REFERENCES

1. Kent, R. D.; Vikesland, P. J. Controlled Evaluation of Silver Nanoparticle Dissolution Using Atomic Force Microscopy. *Environ. Sci. Technol.* **2012**, *46*, 6977-6984.
2. Zhang, X. Y.; Hicks, E. M.; Zhao, J.; Schatz, G. C.; Van Duyne, R. P. Electrochemical Tuning of Silver Nanoparticles Fabricated by Nanosphere Lithography. *Nano Lett.* **2005**, *5*, 1503-1507.
3. Hsu, M.-S.; Cao, Y.-W.; Wang, H.-W.; Pan, Y.-S.; Lee, B.-H.; Huang, C.-L. Time-Dependent Surface Plasmon Resonance Spectroscopy of Silver Nanoprisms in the Presence of Halide Ions. *Chemphyschem* **2010**, *11*, 1742-1748.

FIGURES

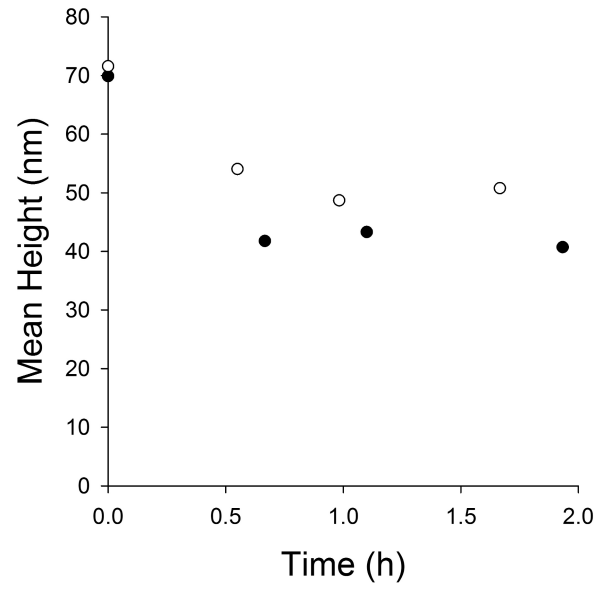


Figure B-1. Time series of mean heights measured by AFM for two CuO/Cu(OH)₂ specimens (pH 5.6, 2 mL/min flow rate).

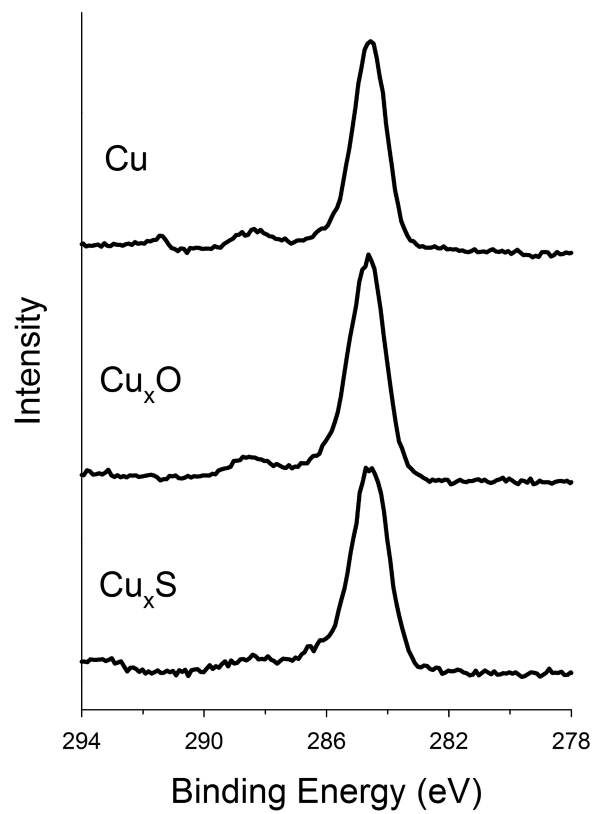


Figure B-2. XPS spectra of the C 1s binding region.

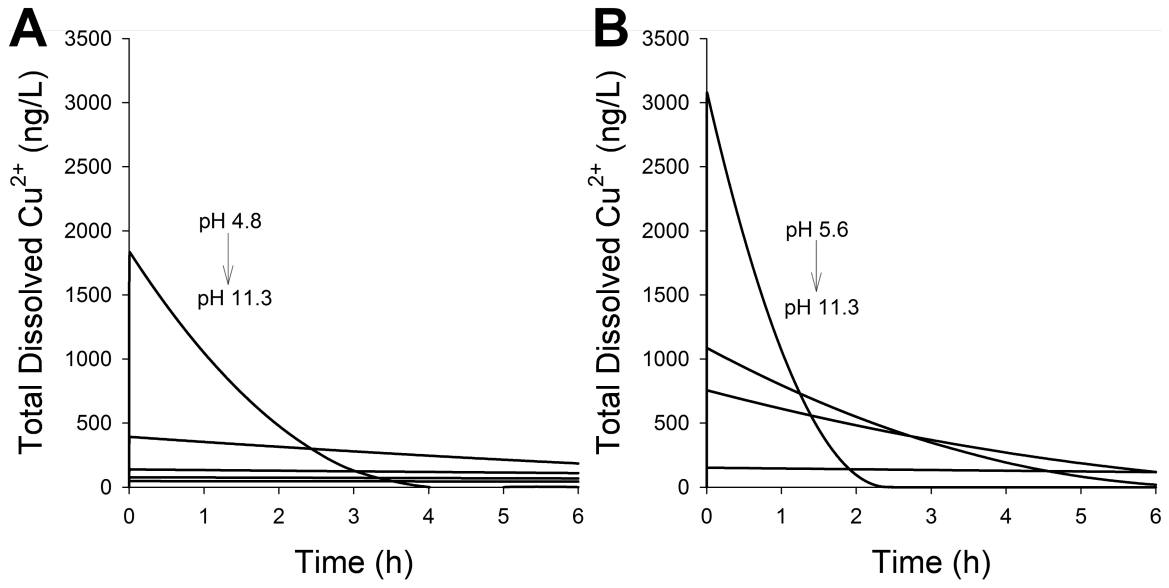


Figure B-3. Modeled concentrations of total dissolved Cu^{2+} for A) Cu NPs and B) CuO/Cu(OH)₂ NPs.

TABLE

Table B-1. Comparison of Dissolved Concentrations and Solubility

pH	Calculated Total Dissolved Cu ²⁺ (ng/L)		Tenorite
	Cu NPs	CuO/Cu(OH) ₂ NPs	Solubility (ng/L)
4.8	1840	-	2,159,801,448
5.6	392	3096	44,872,372
6.6	138	1088	470,584
8.4	77	756	705
11.3	47	151	1,746

Appendix C: Ion Diffusion in Batch Dissolution Experiments

Some of our dissolution experiments were performed in a batch setup in which the prepared specimens were placed in 15-mL polystyrene sample tubes and submerged in 10 mL of an experimental solution. Because the nanoparticles were not suspended and there was no flow or mixing, this experimental setup resulted in a diffusive gradient of dissolved metal ions. Because there is potential for precipitation, the question arises, how concentrated do the ions become near the sample surface in such a system? The answer to this question can be estimated by an application of Fick's laws of diffusion. The sample tubes are long relative to their diameter, so we use the one-dimensional diffusion equation:

$$\frac{\partial[M^{z+}]}{\partial t} = D \frac{\partial^2[M^{z+}]}{\partial x^2}$$

where x is the length along the longitudinal axis of the sample tube, t is time, D is the diffusion coefficient of the metal ion, and $[M^{z+}]$ is the dissolved ion concentration as a function of x and t . The nanoparticle specimen is located at $x = 0$, and the tube has length L and cross-sectional area A . The initial condition for all values of x is $[M^{z+}] = 0$. We assume the nanoparticles are hemispheres so that we can use the contracting sphere rate law, and we assume that they have a perfectly uniform size distribution. At one end of the tube, the nanoparticles are dissolving and releasing metal ions, and at the other end of the tube the diffusion is restrained by the air-water interface; hence, the boundary conditions are

$$\frac{\partial[M^{z+}](x = 0)}{\partial x} = -\frac{3N_0}{DA\tau_L} \left(1 - \frac{t}{\tau_L}\right)^2$$
$$\frac{\partial[M^{z+}](x = L)}{\partial x} = 0$$

where τ_L is the particle lifetime and N_0 is the total number of moles of metal atoms initially present on the substrate. For $t > \tau_L$, the first boundary condition is also set equal to zero. This homogeneous partial differential equation with a non-homogeneous, variable boundary condition can be converted to a non-homogeneous partial differential equation with homogeneous boundary conditions that can be solved analytically by the method of eigenfunction expansion.

The solution for $0 \leq t \leq \tau_L$ is

$$[M^{z+}] = \frac{3N_0x}{DA\tau_L} \left(\frac{x^2}{2L} - 1 \right) \left(1 - \frac{t}{\tau_L} \right)^2 + \sum_{n=0}^{\infty} a_n \cos \frac{n\pi x}{L}$$

where the coefficients a_n are given by

$$a_{n=0} = \frac{N_0L}{DA\tau_L} + \frac{3N_0t}{AL\tau_L} \left(1 - \frac{t}{\tau_L} + \frac{1}{3} \left(\frac{t}{\tau_L} \right)^2 \right) - \frac{2N_0Lt}{DA\tau_L^2} \left(1 - \frac{t}{2\tau_L} \right)$$

$$a_{n>0} = \frac{6N_0L}{DA\tau_L n^2 \pi^2} \left(\frac{2L^2}{D\tau_L n^2 \pi^2} \left(\left(\frac{L^2}{D\tau_L n^2 \pi^2} + 1 \right) (1 - e^{-Dt(n\pi/L)^2}) - \frac{t}{\tau_L} \right) - e^{-Dt(n\pi/L)^2} \right)$$

For $t > \tau_L$, the problem has homogeneous boundary conditions and can be solved by separation of variables to yield

$$[M^{z+}] = \frac{N_0}{AL} + \sum_{n=1}^{\infty} a_n e^{-Dt(n\pi/L)^2} \cos \frac{n\pi x}{L}$$

where the coefficients a_n are in this case given by

$$a_n = \frac{6N_0L}{DA\tau_L n^2 \pi^2} \left(\frac{2L^2}{D\tau_L n^2 \pi^2} \left(\frac{L^2}{D\tau_L n^2 \pi^2} (e^{D\tau_L(n\pi/L)^2} - 1) - 1 \right) - 1 \right)$$

Figure C-1 shows the use of these equations for estimating dissolved ion concentrations for our original experiments with silver nanoparticles (Ag NPs) in NaCl solutions. For these calculations, $N_0 = 4$ nmol, $D = 1.2 \times 10^{-5}$ cm²/s, $A = 1.6$ cm², $L = 6.25$ cm, and the initial AgNP height was 60 nm. The values of the rate constant, k , varied from 0.4 to 2.2 nm/d in our study,

and τ_L is calculated accordingly. The final concentrations were converted to units of $\mu\text{g/L}$. The assumption that the particles have a perfectly uniform size distribution makes the modeled metal ion generation rate an overestimate because in reality the 4 nmol of metal initially on the substrate is mostly ($\sim 75\%$) in the form of metal films and large, irregular nanostructures that are the result of defects in the lithographic mask of latex spheres used in the fabrication process. These films and irregular structures have a much lower surface area to mass ratio than the uniform nanoparticles that are emphasized in this study; thus, their mass-based dissolution rate is slower than that of the nanoparticles—but the model assumes that 100% of the metal mass on the substrate consists of the nanoparticles with the higher mass-based dissolution rate.

The modeled concentrations shown in Figure C-1 indicate that the dissolved ion concentrations near the substrate surface in our batch experiments are quite low indeed in spite of the concentration gradients. Comparing the maximum Ag^+ concentrations at the substrate surface with the solubility of AgCl for the different conditions illustrates this point. In 550 mM NaCl , $k = 2.2$ nm/d. The maximum predicted concentration for this condition is 57 $\mu\text{g/L}$, but the solubility of AgCl in 550 mM NaCl is 3100 $\mu\text{g/L}$. In 10 mM NaCl , $k = 0.4$ nm/d. The actual experiments only ran for 2 weeks, and the maximum concentration at the substrate surface after 2 weeks is less than 20 $\mu\text{g/L}$ for this condition. The solubility of AgCl in 10 mM NaCl is 80 $\mu\text{g/L}$. Again, 20 $\mu\text{g/L}$ is an overestimate, so the actual dissolved ion concentration near the AgNP surfaces was well below the solubility limit.

FIGURE

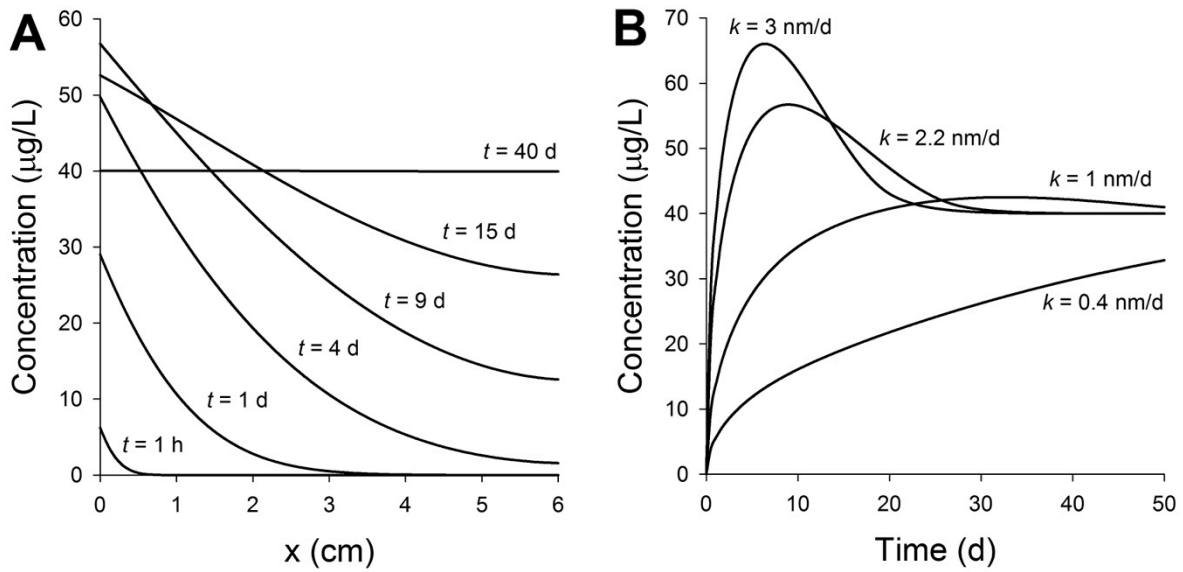


Figure C-1. A) Modeled dissolved Ag^+ concentration profiles at various times along the longitudinal axis of a sample tube during a batch dissolution experiment with $k = 2.2 \text{ nm/d}$. B) Modeled dissolved Ag^+ concentration as a function of time at the sample surface (i.e., at $x = 0$) for various dissolution rate constants.